Ph.D. DISSERTATION

Highly Sensitive Interface Circuit with Complementary Gas Sensors

상보적인 감지 특성을 갖는 가스 센서들로 구성된 고민감성 인터페이스 회로

by

YUJEONG JEONG

February 2023

DEPARTMENT OF ELECTRICAL AND
COMPUTER ENGINEERING
COLLEGE OF ENGINEERING
SEOUL NATIONAL UNIVERSITY

Highly Sensitive Interface Circuit with Complementary Gas Sensors

상보적인 감지 특성을 갖는 가스 센서들로 구성된 고민감성 인터페이스 회로

지도교수 최 우 영

이 논문을 공학박사 학위논문으로 제출함

2023 년 2 월

서울대학교 대학원

전기 · 정보공학부

정 유 정

정유정의 공학박사 학위논문을 인준함

2023 년 2 월

위 원 장 : 장 호 원 (인)

부위원장 : 최 우 영 (인)

위 원 : 이 종 호 (인)

위 원 : 권 혁 인 (인)

위 원 : 배 종 호 (인)

Highly Sensitive Interface Circuit with Complementary Gas Sensors

by

Yujeong Jeong

Advisor: Woo Young Choi

A dissertation submitted in partial fulfillment of

the requirements for the degree of

Doctor of Philosophy

(Electrical and Computer Engineering)

in Seoul National University

February 2023

Doctoral Committee:

Professor Ho Won Jang, Chair

Associate Professor Woo Young Choi, Vice-Chair

Professor Jong-Ho Lee

Professor Hyuck-In Kwon

Assistant Professor Jong-Ho Bae

ABSTRACT

Recently, with the rapid development of industrialization, indoor and outdoor air pollution has deteriorated due to harmful gases emitted from transportation and building materials. Accordingly, there is an increasing need for gas sensing systems to monitor indoor and outdoor air quality. With this increased demand, many research groups have studied various gas sensor platforms, such as optical, electrochemical, and semiconductor-type gas sensors. Among them, resistor-type gas sensors have been mainly studied since they have the advantages of large response, simple process, and low cost. However, the resistor-type gas sensor has a disadvantage in that the size and power consumption of the sensor should be increased for sufficient operating current and sensitivity. Thus, our research group proposed a FET-type gas sensor with a horizontal floating-gate to solve this limitation of the resistor-type sensor. The FET-type gas sensor can operate with low power and integrate with CMOS-based interface circuits and processors since it is compatible with conventional CMOS-based processes.

In this dissertation, interface circuits using a gas sensor platform compatible with conventional CMOS processes are proposed. The gas sensor platform includes FET-type gas sensors with *n*- and *p*-channel, FET elements, and resistor-type gas sensors fabricated on the same substrate. Especially in this dissertation, interface circuits composed of complementary gas sensors are proposed. The current of the complementary gas sensors is changed in opposite directions in the same gas response. We compare the characteristics of various amplifier circuits in terms of sensitivity and signal-to-noise ratio (SNR) to prove the superiority of the amplifier circuit composed of complementary gas sensors. Also, the electrical and sensing characteristics of an inverter circuit with *n*FET- and *p*FET-type gas sensors are investigated. The pulse width modulated behavior of the inverter circuit is also confirmed. The pulse width of the output voltage in the inverter circuit is adjusted according to the type and concentration of the gas molecules.

The proposed interface circuit with gas sensors prevents an increase in noise and power consumption in the transmission of the sensor signal to the interface circuit since the gas sensor and interface circuits are fabricated on the same substrate. Also, the pulse width modulated behavior of the inverter circuit is expected to be the basis for future intelligent gas sensing systems.

Keywords: FET-type gas sensor, Amplifier circuit, CMOS, Inverter circuit, Complementary, Low frequency noise

Student number: 2017-24278

CONTENTS

Abstract..i

Contents..iii

List of Figures..vi

Chapter 1

Introduction..1

1.1 Study background..1

1.1.1 Gas sensing technology..1

1.1.2 Interface circuit of gas sensors..4

1.2 Purpose of research..8

1.3 Dissertation outline..10

Chapter 2

Circuit structure and fabrication....................................12

2.1 Circuit structure..12

2.2 Circuit fabrication..16

Chapter 3

Characteristics of amplifier circuits..................................20

3.1 Electrical and sensing characteristics of unit sensors....................20

3.2 Electrical characteristics of amplifier circuits...............................32

3.3 Sensing characteristics of amplifier circuits.................................37

3.4 Low frequency noise characteristics of amplifier circuits...........47

Chapter 4

Characteristics of inverter circuit....................................57

4.1 Electrical and sensing characteristics of inverter circuit................57

4.2 Application of inverter circuit..64

Chapter 5

Conclusions..69

Appendix A

Various sensing materials………………….........................72

A.1 Tungsten disulfide (WO_3)..72

A.2 Graphene quantum dots (GQDs)...74

Bibliography..78

Abstract in Korean..86

List of Publications..88

List of Figures

Figure 1.1. Top scanning electron microscopy (SEM) image and schematic view of an HFGFET-type gas sensor [31]. ……………………………………….…..……6

Figure 1.2. Configuration of the voltage dividing circuit and Wheatstone bridge circuit with a resistor-type gas sensor. …..………………………….....................7

Figure 1.3. Configuration of the transresistance amplifier (TRA) circuit with a resistor-type gas sensor. ...…………………………………….…….....................7

Figure 2.1. Top SEM image and 3-D schematic birds' eye view of the amplifier circuit composed of the FET-type gas sensor with (a)-(b) FET load and (c)-(d) resistor-type gas sensor. (e) Microscopic image and (f) 3-D schematic birds' eye view of the CMOS inverter circuit composed of the *n*FET- and *p*FET-type gas sensors. .....……………………………………………………………….......14

Figure 2.2. (a) 3-D schematic birds' eye view of the *n*FET- and *p*FET-type gas

sensors, FET load, and resistor-type gas sensors in the proposed interface circuits. Cross sectional view of the (b) *n*FET- and (c) *p*FET-type gas sensors cut along A-A' and B-B', respectively. 15

Figure 2.3. (a) SEM image and (b) EDS spectrum of the In_2O_3 sensing layer deposited on the gas sensors. 15

Figure 2.4. Fabrication process flow of the Si CMOS gas sensor platform constituting interface circuits. Here, (a)-(h) correspond to Fig. 2.5(a)-(h). 16

Figure 2.5. (a)-(f) Cross sectional view of the fabrication process of the Si CMOS-based interface circuit with gas sensors. 19

Figure 3.1. I_D-V_{CG} curves of the fabricated (a) *n*FET-type and (b) *p*FET-type gas sensor as a parameter of the operating temperature (20 ºC ~160 ºC). 22

Figure 3.2. I_D-V_{CG} curves of the fabricated (a) *n*FET and *n*FET-type gas sensor and (b) *p*FET and *p*FET-type gas sensor at 20 ºC and 160 ºC. 23

Figure 3.3. Program/Erase characteristics of the (a) *n*FET- and (b) *p*FET-type gas

sensors under the different V_{PGM} and V_{ERS} at 20 ºC. ……………………...............…24

Figure 3.4. I-V characteristics of the fabricated resistor-type gas sensor with In_2O_3 sensing layer at 20 ºC and 160 ºC. …………………….……………….............…25

Figure 3.5. Energy band diagram of the fabricated FET-type gas sensor when exposed to air and NO_2 gas ambience. $\Delta\rho$ is additionally introduced below. ……....27

Figure 3.6. Transient sensing characteristics of the (a) nFET-type and (b) pFET-type gas sensor as a parameter of NO_2 gas concentration (0 ppb ~ 400 ppb) at 160 ºC. Here, $V_{CG} = V_{th} \pm 0.3$ V and $V_{DS} = \pm 0.1$ V. ………….………………...........28

Figure 3.7. Transient sensing characteristics of the resistor-type gas sensor as a parameter of NO_2 gas concentration (0 ppb ~ 400 ppb) at 160 ºC. …….…..…..…..29

Figure 3.8. Response of nFET-type and pFET-type gas sensors and a resistor-type gas sensor versus NO_2 concentration. All responses follow Langmuir theory. …...29

Figure 3.9. Transient sensing characteristics of the (a) nFET-type and (b) pFET-type gas sensor as a parameter of H_2S gas concentration (25 ppm ~ 50 ppm) at 180

°C. ……………………………………………………………….……………………30

Figure 3.10. Transient sensing characteristics of the resistor-type gas sensor as a parameter of H_2S gas concentration (25 ppm ~ 50 ppm) at 180 °C. ……….…..…31

Figure 3.11. (a) Transfer curves (V_{out}-V_{in}) and (b) voltage gain (= V_{out}/V_{in}) of the *n*-type amplifier circuit with FET load as a parameter of V_b (0.6 V ~ 1.6 V). The V_b is a bias voltage applied to the CG of the *n*FET load. At V_b = 0.8 V and V_{in} = 0.12 V, the amplifier circuit has maximum gain. ……………………………….……...34

Figure 3.12. (a) Transfer curves (V_{out}-V_{in}) and (b) voltage gain (= V_{out}/V_{in}) of the *p*-type amplifier circuit with FET load as a parameter of V_b (-0.8 V ~ -1.4 V). The V_b is a bias voltage applied to the CG of the *n*FET load. At V_b = -1.0 V and V_{in} = -0.26 V, the amplifier circuit has maximum gain. ………………..…………..……...35

Figure 3.13. Transfer curves (V_{out}-V_{in}) and voltage gain (= V_{out}/V_{in}) of (a) the *n*-type amplifier circuit with R-type sensor and (b) the *p*-type amplifier circuit with R-type sensor at 160 °C. The maximum voltage gain of the *n*- and *p*-type amplifier circuits

are 4.78 V/V at V_{in} = 0.12 V and 4.82 V/V at V_{in} = 0.24 V, respectively. 36

Figure 3.14. (a) Transfer curves of the amplifier circuit consisting of an *n*FET-type gas sensor and an *n*FET load as a parameter of NO_2 concentration. The inset shows the circuit diagram of the amplifier circuit. (b) $V_{out,gas}$ - $V_{out,air}$ of the *n*-type amplifier circuit with FET load versus V_{in} as a parameter of NO_2 concentration. 41

Figure 3.15. (a) Transfer curves of the amplifier circuit consisting of a *p*FET-type gas sensor and a *p*FET load as a parameter of NO_2 concentration. The inset shows the circuit diagram of the amplifier circuit. (b) $V_{out,gas}$ - $V_{out,air}$ of the *p*-type amplifier circuit with FET load versus V_{in} as a parameter of NO_2 concentration. 42

Figure 3.16. $V_{out,gas}$ - $V_{out,air}$ of the (a) *n*-type amplifier circuit and (b) *p*-type amplifier circuit with FET load versus NO_2 concentration as a parameter of V_{in}. The curves in these figures follow the Langmuir's theory. 43

Figure 3.17. (a) Transfer curves of the amplifier circuit consisting of the *n*FET- and resistor-type gas sensors as a parameter of NO_2 concentration. The currents of both sensors in the amplifier circuit change in same direction by the NO_2 gas reaction.

(b) $V_{out,gas}$ - $V_{out,air}$ of the n-type amplifier circuit with resistor-type sensor versus V_{in} as a parameter of NO_2 concentration. 44

Figure 3.18. (a) Transfer curves of the amplifier circuit consisting of the pFET- and resistor-type gas sensors as a parameter of NO_2 concentration. The currents of both sensors in the amplifier circuit change in opposite directions by the NO_2 gas reaction. (b) $V_{out,gas}$ - $V_{out,air}$ of the p-type amplifier circuit with resistor-type sensor versus V_{in} as a parameter of NO_2 concentration. 45

Figure 3.19. $V_{out,gas}$ - $V_{out,air}$ of (a) the n-type and (b) p-type amplifier circuit with R-type sensors versus NO_2 concentration. The $|V_{out,gas}$ - $V_{out,air}|$ versus NO_2 concentration in the n-type circuit is close to linear (R^2= 0.989) at V_{in} = -0.42 V and its slope is 0.582 mV/ppb. The $V_{out,gas}$ - $V_{out,air}$ in the p-type circuit is close to linear (R^2= 0.985) at V_{in} = 0.66 V and its slope is 2.2 mV/ppb. 46

Figure 3.20. (a) Normalized current noise power spectral densities (S_I/I^2s) of resistor-type sensor and n^+ poly-Si resistor measured at 160 °C. The resistor-type sensor with an In_2O_3 sensing material exhibits 1/f noise behavior. (b) The log-log plot of S_I sampled at 10 Hz versus I. 52

Figure 3.21. (a) Normalized drain current noise power spectral densities (S_{ID}/I_D^2s) of the nFET-type and pFET-type sensors measured at $V_{CG} = V_{th}$ and 160 °C. (b) The log-log plot of S_{ID}/I_D^2s sampled at 10 Hz versus I. 53

Figure 3.22. $V_{out,gas}$ - $V_{out,air}$ and the output voltage noise (S_{Vout}) of the (a) n-type and (b) p-type amplifier circuits with FET loads as a function of V_{in} at 160 °C. The S_{Vout} of the n-type amplifier circuit shows no dependence on V_{in}. The S_{Vout} of the p-type amplifier circuit is minimum when V_{in} is 0 V. 54

Figure 3.23. (a) $|V_{out,gas}$ - $V_{out,air}|$ and (b) the output voltage noise (S_{Vout}) of the n-type and p-type amplifier circuits with resistor-type sensors versus V_{in} at 160 °C. The S_{Vout}s of the amplifier circuits are mainly determined by the noise of the resistor-type gas sensor. 55

Figure 3.24. SNR of four different amplifier circuits versus V_{in}. The noise and output signal of each circuit is measured at 160 °C. 56

Figure 4.1. Transfer (V_{out}-V_{in}) curves of the fabricated CMOS inverter with nFET- and pFET-type gas sensor as a parameter of the V_{DD} at room temperature. 60

Figure 4.2. Schematic illustration deriving operating points of the CMOS inverter circuit before and after NO_2 gas response using load-line analysis. 60

Figure 4.3. (a) Transfer curves of the inverter circuit consisting of the *n*FET- and *p*FET-type gas sensors as a parameter of NO_2 concentration (0 ppb ~ 500 ppb) at 120 ºC. (b) ΔV_{out} (= $V_{out,gas}$ - $V_{out,air}$) of the inverter circuit versus V_{in} as a parameter of NO_2 concentration. 61

Figure 4.4. Schematic illustration deriving operating points of the CMOS inverter circuit before and after H_2S gas response using load-line analysis. 62

Figure 4.5. (a) Transfer curves of the inverter circuit consisting of the *n*FET- and *p*FET-type gas sensors as a parameter of H_2S concentration (0 ppm ~ 50 ppm) at 160 ºC. (b) ΔV_{out} (= $V_{out,gas}$ - $V_{out,air}$) of the inverter circuit versus V_{in} as a parameter of H_2S concentration. 63

Figure 4.6. (a) Circuit schematic of the inverter circuit composed of the FET-type gas sensors for PWM operation. (b) Pulse schematic diagram of input voltage (V_{in})

and V_{out} with different switching thresholds. When a triangular wave is applied to the input of the inverter circuit, the pulse width of the output voltage (V_{out}) is determined by the switching threshold. ....……………...66

Figure 4.7. (a) Input voltage (V_{in}) and (b) output voltage (V_{out}) in the transient analysis of the CMOS inverter circuit when exposed to different concentrations of the NO_2 gas (0 ppb ~ 500 ppb). In Fig. 4.7(a), dotted lines indicate the switching threshold of the circuit as a parameter of the NO_2 gas concentration. 67

Figure 4.8. (a) Input voltage (V_{in}) and (b) output voltage (V_{out}) in the transient analysis of the CMOS inverter circuit when exposed to different concentrations of the H_2S gas (0 ppm ~ 50 ppm). In Fig. 4.8(a), dotted lines indicate the switching threshold of the circuit as a parameter of the H_2S gas concentration. 68

Figure A.1. Transient sensing characteristics of the FET-type gas sensor with WO_3 sensing layer at 180 ºC. The WO_3 sensing layer of the gas sensor is deposited at an oxygen flow rate of 3 sccm with 30 sccm argon gas in the sputtering process. 73

Figure A.2. Comparison of the response of the FET-type gas sensor to the three different gases (NO_2, H_2S, and SO_2). The concentration of the NO_2 gas is 500ppb, and that of other gases is 50 ppm. 74

Figure A.3. Transfer curves (I_D-V_{CG}) of the FET-type humidity sensor as a parameter of the relative humidity (from 17.5% RH to 81.3% RH) at 20 ℃. 77

Figure A.4. Long-term stability of the humidity sensor to the humid air. The response of the humidity sensor has no noticeable variation in all ranges of relative humidity levels even after more than five months. …..77

Chapter 1

Introduction

1.1 Study background

1.1.1 Gas sensing technology

Recently, many people have been exposed to harmful gases daily as indoor and outdoor air quality has deteriorated. With rapid industrialization and socialization, toxic gases are emitted from automobiles and factories outdoors, and VOC gases from building materials are emitted indoors [1-3]. These toxic gases from air pollution cause several diseases, such as sickhouse syndrome [4-5]. In addition, demand for gas sensors is increasing in various fields, such as food freshness checks and diagnosing people's diseases [6-7]. Requirements such as mobility, selectivity, long-term reliability, and price should be met for the application of gas sensors in various fields. Many research groups have studied various types of gas sensors, such as optical [8-10], electrochemical [11-13], and semiconductor-type [14-16], to satisfy these requirements.

At a specific light source wavelength, the gas molecules have their own absorption characteristics. Therefore, the optical gas sensor detects target gas using the principle that only a specific wavelength of light is absorbed by the gas molecules when exposed to various wavelengths of light sources [17]. The optical gas sensor has the advantage of high selectivity and fast response time since the optical gas sensor operates according to the intrinsic properties of the gas without a chemical reaction between the gas molecules and the gas sensor [18]. On the other hand, the optical gas sensor has limitations in terms of size, portability, and price. Electrochemical gas sensors detect gas molecules by redox reactions at the electrode [19]. The redox reaction at the working electrode causes the current of potential difference between the working electrode and the reference electrode. Electrochemical gas sensors have the advantage of being sensitive to low concentrations of gas molecules. However, since the electrochemical gas sensor uses an electrolyte, it has a short lifespan and requires periodic maintenance of the electrolyte [20].

A semiconductor-type gas sensor detects a target gas using a sensing material whose electrical properties change by the reaction between the gas molecules and the sensing material. Among semiconductor-type gas sensors, a resistor-type gas sensor has been studied the most because of its simple fabrication process and low price. Various sensing materials, such as metal oxides (MOX) [21-23], carbon nanomaterials [24-26], and Transition Metal Dichalcogenides (TMDCs) [27-29], have been applied to the resistor-type gas sensor. However, the resistor-type gas sensor has a large size for sufficient operating current and sensitivity, which also increases power consumption [30]. In addition, the resistor-type sensor is incompatible with the conventional silicon-based CMOS process. To overcome the limitations, our laboratory has proposed a horizontal floating gate FET-type gas sensor, as shown in Fig 1.1 [31,32]. The FET-type gas sensor has a horizontal floating-gate (FG) interdigitated with a control-gate (CG), so it has a high coupling ratio. In addition, the FET-type gas sensor can be operated with low power consumption using a micro-heater that locally heats the sensing layer [33]. Especially the FET-type gas sensor can be integrated with CMOS-based interface circuits and processors since it is compatible with the conventional CMOS process [34].

1.1.2 Interface circuit of gas sensors

Gas sensing systems roughly consist of gas sensors, interface circuits, and processors [35,36]. In the gas sensing system, the gas sensors detect gas molecules and generate and transfer the sensing signal to the interface circuits. The interface circuits amplify and pre-process the signal from the gas sensors and transfer it to the processor. Most semiconductor-type gas sensors are incompatible with the conventional silicon (Si) CMOS process [36]. Thus, there are not enough studies to integrate the gas sensors with the CMOS-based interface circuits and the processors. For this reason, the gas sensors are manufactured separately from the CMOS-based interface circuits and processors in the conventional gas-sensing system. However, as the signal is transmitted to the processor through many interface circuits, the signal noise increases and the power consumed by the gas-sensing system also increases [36]. Therefore, it is essential to integrate the gas sensor and CMOS circuitry on the same substrate to analyze the sensor signal more stably and accurately [36]. Also, integrating the gas sensor and CMOS circuitry is advantageous for mass production, making the unit chip cheaper.

In the gas response, most conventional semiconductor-type gas sensors produce a current signal. However, as mentioned above, the noise of the sensor signal increases as it passes through the interface circuit. Thus, a voltage signal is preferred over the current signal for superior noise immunity of the sensor signal [37]. The most studied resistor-type gas sensors convert the current signal to the voltage signal using a voltage dividing or Wheatstone bridge circuit, as shown in Fig. 1.2 [38-40]. The voltage-dividing circuit can be fabricated by a simple fabrication process. To accommodate significant fluctuations in the resistance of the sensing material, the circuit should use a reference resistor with considerable resistance [40]. Also, simple circuits such as voltage dividing and bridge circuits cannot be used due to dynamic range limitations in the interface circuits. Thus, complex multi-scale circuits such as transresistance amplifier (TRA) are used, which consume a lot of power, as shown in Fig. 1.3. The reported TFT-type gas sensor uses a fixed resistor or TFT load to consist of an amplifier circuit for conversion to a voltage output [41-43]. The amplifier circuit using a fixed resistor has a limitation: a resistor should be manufactured separately from the TFT-type gas sensors [41]. In the reported amplifier circuits, since the TFT load is fabricated using TFT sensors with a passivation layer, it is large and incompatible with the CMOS process [42].

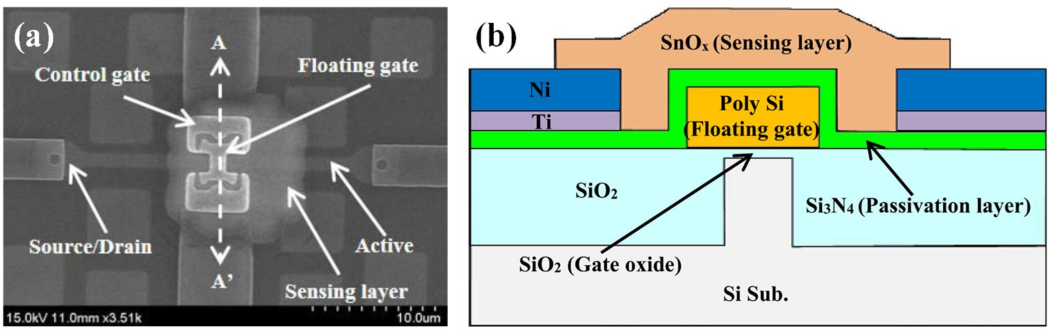

Fig. 1.1. Top scanning electron microscopy (SEM) image and schematic view of an HFGFET-type gas sensor [31].

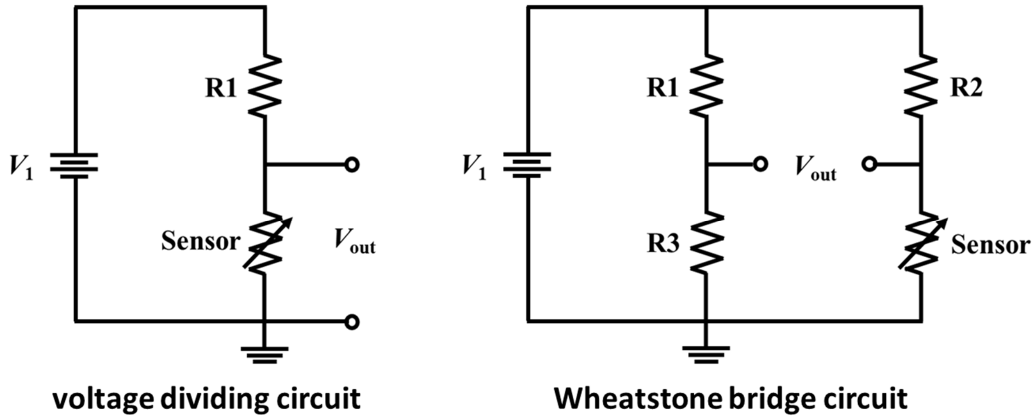

Fig. 1.2. Configuration of the voltage dividing circuit and Wheatstone bridge circuit with a resistor-type gas sensor.

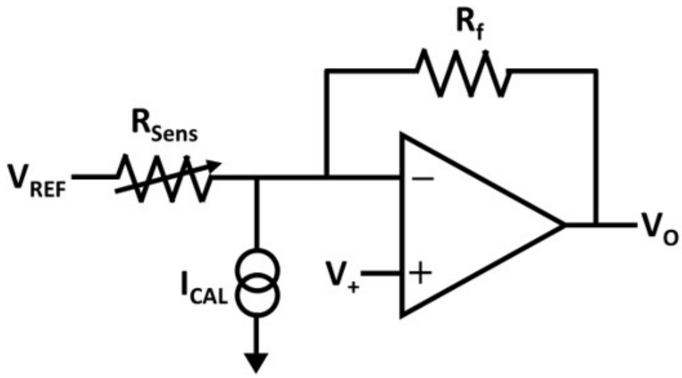

Fig. 1.3. Configuration of the transresistance amplifier (TRA) circuit with a resistor-type gas sensor.

1.2 Purpose of research

The interface circuit of the gas sensing system has been studied separately from the gas sensor since most gas sensors are incompatible with the conventional Si CMOS process. However, as mentioned above, research is needed to integrate the interface circuit and the gas sensor on the same substrate due to increased noise and power consumption. Moreover, it is necessary to study the interface circuit related to the gas sensor to implement an intelligent sensor system such as neuromorphic computing or in-sensor computing technology. So far, some simple amplifier circuits with a gas sensor have been studied, but the circuit configuration is limited because of their incompatibility with the CMOS process. Since the gas sensor platform proposed by our research group is compatible with the Si CMOS process, various circuit configurations can be fabricated.

In this dissertation, interface circuits composed of complementary sensors are proposed—a current of the complementary sensors changes in the opposite direction in the gas response. The proposed interface circuits are fabricated using Si CMOS process technology. Thus, the *n*FET-, *p*FET-, resistor-type gas sensors, and FET elements can be fabricated with only 10 photomasks on the same substrate. First, the excellence of the amplifier circuit with complementary sensors is demonstrated by comparing the electrical and gas sensing characteristics of different amplifier circuits. In addition, the signal-to-noise ratio of the amplifier circuit is derived by analyzing the low-frequency noise characteristics. The electrical and gas sensing characteristics of the inverter circuit composed of *n*FET- and *p*FET-type sensors are also analyzed. Moreover, the pulse width modulated operation according to the type and concentration of the gas molecules is proposed using the inverter circuit with gas sensors. Finally, it is verified that various sensing materials can be introduced into the interface circuit by investigating the sensing characteristics of the gas sensor with various sensing materials.

1.3 Dissertation outline

This dissertation is organized as follows. Chapter 1 presents the need for gas sensor technology and introduces various types of gas sensors. Then, the need for research to integrate CMOS-based interface circuits and processors with gas sensors is covered. Moreover, the limitations of conventional studies on interface circuits composed of gas sensors are presented in this chapter. The purpose of the research and the outline of the dissertation are also provided, respectively. Chapter 2 describes the structure and fabrication process of the CMOS-based interface circuit composed of the FET- and resistor-type gas sensors with the CMOS transistors sensors. Chapter 3 presents the electrical and sensing characteristics of the fabricated *n*FET-, *p*FET-, and resistor-type gas sensors. Then, the electrical and sensing characteristics of the amplifier circuit composed of the FET-type gas sensors with the resistor-type gas sensor or FET load are investigated. Moreover, low-frequency noise characteristics of the amplifier circuits are also investigated in this chapter. In chapter 4, the electrical and sensing characteristics of the inverter circuit composed of the *n*FET- and *p*FET-type gas sensors are described. Moreover, this chapter contains the application of the inverter circuit for pulse width modulated behavior. Finally, Chapter 6 presents the conclusion of the study.

Chapter 2

Circuit structure and fabrication

2.1 Circuit structure

Figs. 2.1 show the top SEM image and 3-D schematic birds' eye view of the interface circuits composed of different types of gas sensors. Fig. 2.1(a) and (b) show the top SEM image and 3-D schematic birds' eye view of the amplifier circuit composed of the FET-type gas sensor with FET load. In this amplifier circuit, the FET load has the same type of channel doping as the FET-type gas sensor. The *p*FET-type sensor has complementary sensing characteristics to the resistor- and *n*FET-type sensors. Thus, the amplifier circuit in Fig. 2.1(c) and (d) consists of the FET- and resistor-type gas sensor. Fig. 2.1(e) and (f) show the microscopic image and 3-D schematic birds' eye view of the CMOS inverter circuit composed of the *n*FET- and *p*FET-type gas sensors. The *n*FET-, *p*FET-, resistor-type sensors, and FET elements constituting these interface circuits are fabricated on the same substrate using a standard 0.5 μm Si CMOS process technology. Figs. 2.2 show the 3-D schematic birds' eye view of the *n*FET- and *p*FET-type gas sensors and FET load and resistor-type gas sensors in the interface circuits. As shown in Fig. 2.2, the horizontal placement and interdigitation of the control-gate (CG) and floating-gate (FG) in the FET-type gas sensors. The coupling ratio of the FET-type gas sensors is increased by the interdigitated pattern of the CG and FG.

The sensing layers of the gas sensors in the interface circuits are deposited simultaneously. Also, it is possible to use different sensing materials for each sensor using additional photomasks. In this dissertation, In_2O_3 films are deposited on the sensing layer of the gas sensors constituting the interface circuits. Fig. 2.3(a) shows the SEM image of the In_2O_3 sensing materials. As shown in Fig. 2.3(a), the target gas can pass through the sensing layer since the sensing layer to reach the In_2O_3/SiO_2 interface is sufficiently porous. Electron dispersive X-ray spectroscopy (EDS) is performed to identify the components of the In_2O_3 sensing layer (Fig. 2.3(b)). The constituents are present in the same composition ratio as the inherent values of In2O3 film, according to the X-ray peak of the EDS.

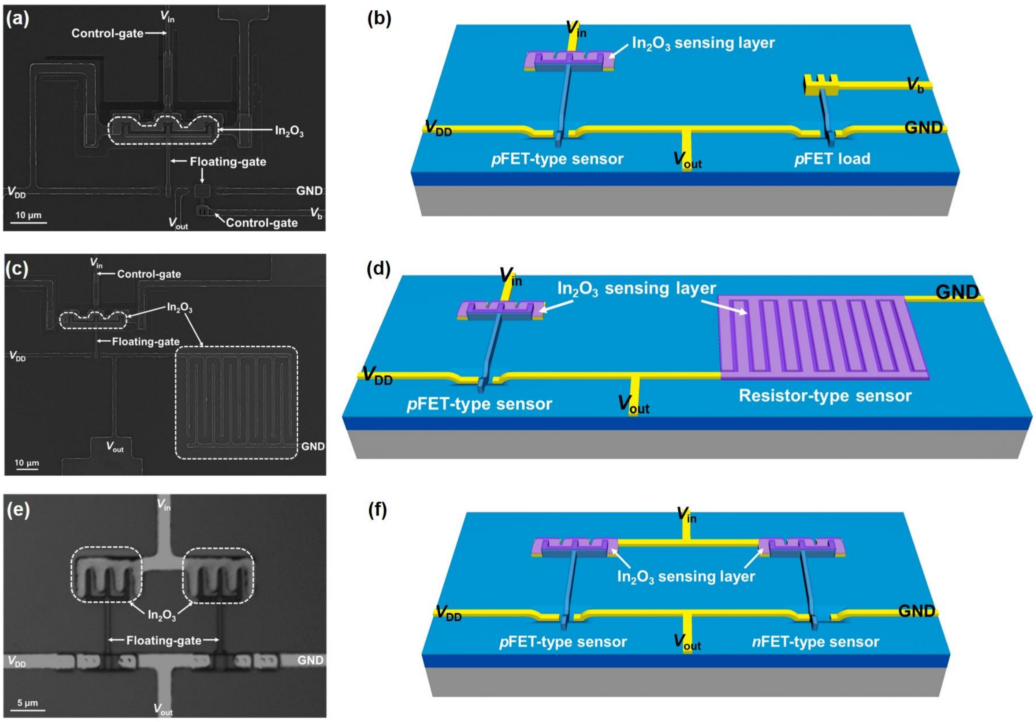

Fig. 2.1. Top SEM image and 3-D schematic birds' eye view of the amplifier circuit composed of the FET-type gas sensor with (a)-(b) FET load and (c)-(d) resistor-type gas sensor. (e) Microscopic image and (f) 3-D schematic birds' eye view of the CMOS inverter circuit composed of the *n*FET- and *p*FET-type gas sensors.

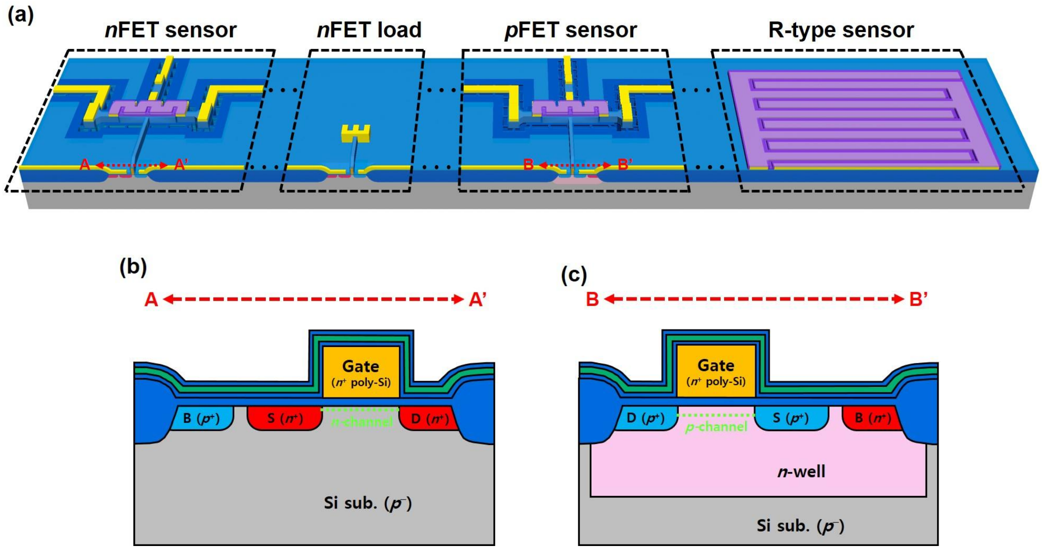

Fig. 2.2. (a) 3-D schematic birds' eye view of the *n*FET- and *p*FET-type gas sensors, FET load, and resistor-type gas sensors in the proposed interface circuits. Cross sectional view of the (b) *n*FET- and (c) *p*FET-type gas sensors cut along A-A' and B-B', respectively.

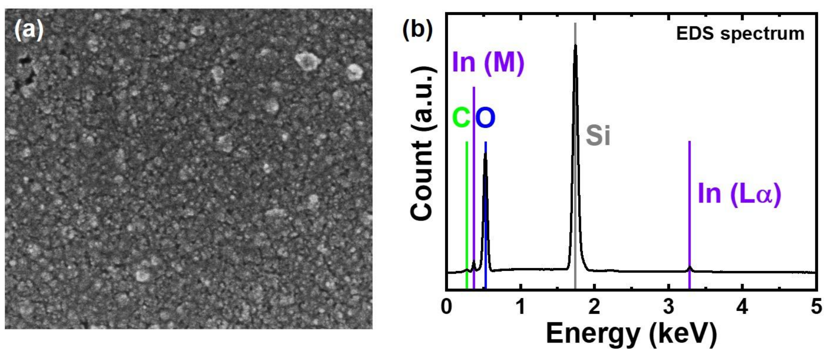

Fig. 2.3. (a) SEM image and (b) EDS spectrum of the In_2O_3 sensing layer deposited on the gas sensors.

2.2 Circuit fabrication

The Si CMOS gas sensor platform constituting interface circuits is fabricated using standard Si CMOS process technology with no more than ten photomasks. Also, *n*FET- and *p*FET-type gas sensors are fabricated on the same substrate using a well formation process. Figs. 2.4 and 2.5 show the key process flow and schematic diagram of the key process steps. The detailed fabrication process of the gas sensor platform is as follows.

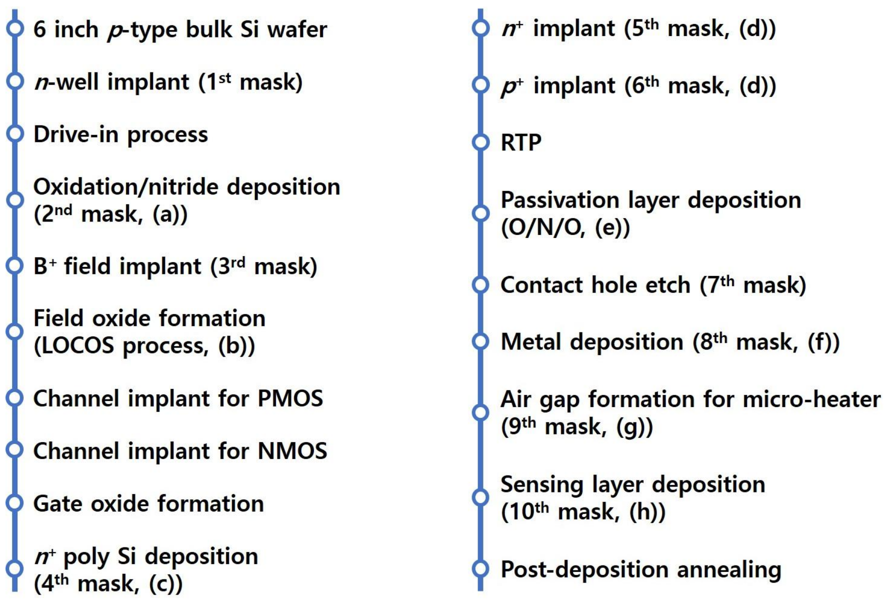

Fig. 2.4. Fabrication process flow of the Si CMOS gas sensor platform constituting interface circuits. Here, (a)-(h) correspond to Fig. 2.5(a)-(h).

The standard wafer cleaning process, including SPM, APM, HPM, and DHF cleaning, was used to clean a 6-inch *p*-type bulk Si wafer with (100) orientation. The reference markers were patterned by the photolithography and inductively coupled plasma (ICP) dry etching processes to align more compactly between the patterns to be formed. Next, the *n*-well formation process was performed for *p*FET-type devices, including *p*FET-type gas sensor and *p*FET load (Fig. 2.5(a)). To create sacrificial oxide, which protects the substrate from damage in the ion implantation process, a 10 nm-thick SiO_2 layer was first formed by low-pressure chemical vapor deposition (LPCVD). After the *n*-well implantation process (P^+, 120 keV, $3x10^{12}$ cm^{-2}), the drive-in process was performed at 1100 °C for 11 h. Then, a 10 nm-thick SiO_2 layer and a 150 nm-thick Si_3N_4 layer were deposited and patterned to define the active regions of the FET. The B^+ field implantation was carried out, which penetrates the thick oxide and increases the doping concentration at the silicon interface, protecting the thick oxide field regions of *n*FET-type devices, including *n*FET-type gas sensor and *n*FET load. As the process of the local oxidation of silicon (LOCOS) technique, a 550 nm-thick SiO_2 layer for the formation of field oxide was thermally grown at 1000 °C for 1h 55 min. After removing the SiO_2 and Si_3N_4 layers, the thermal oxidation process was performed to remove the white-ribbon-shaped residues. Then, the thermal oxide was removed except for a 10 nm-thick sacrificial oxide layer for the channel implantation process (Fig. 2.5(b)). The *n*- and *p*-channel implantation of the FET devices was carried out to adjust the electrical characteristics, including the V_{th} of the FET devices. A 10 nm-thick SiO_2 was thermally grown at 850 ºC for 40 min. And then, a 300 nm-thick n^+ doped poly-Si for FG and micro-heater was deposited by the LPCVD (Fig. 2.5(c)). Then, the arsenic and boron ions are implanted to form source/drain (S/D) regions of the *n*FET- and *p*FET-type devices (Fig. 2.5(d)). The body implantation of the *n*FET- and *p*FET-type devices were simultaneously performed with the S/D implantation of the *p*FET- and *n*FET-type devices, respectively. The rapid thermal process (RTP) was performed, and then, the O/N/O passivation layer (10 nm/20nm/ 10 nm) was deposited by the thermal oxidation and LPCVD (Fig. 2.5(e)). After the contact hole formation, a Ti/TiN/Al/TiN metal stack (20 nm/20 nm/50 nm/10 nm) was deposited by the sputtering method (Fig. 2.5(f)). To make an air gap under the micro-heater of the FET-type gas sensors, the dry etching was performed anisotropically in the first etching process and isotropically in the second etching process. After the formation of the air gap (Fig. 2.5(g)), the H_2 alloy was performed in a 5 % of hydrogen (H_2) ambience at 400 ºC for 10 min.

Finally, the sensing layer is deposited on the interdigitated CG-FG pattern. Since most sensing materials, such as carbon nanomaterials and TMDCs, are incompatible with the conventional Si CMOS process, the sensing layers of the gas sensors in the interface circuits are formed in the final step of the fabrication process. Thus, the CMOS-based sensor platform can be protected from contamination during the formation of the sensing layer. In this dissertation, the In_2O_3 sensing layer is deposited by a radio-frequency (RF) magnetron sputter method (Fig. 2.5(h)). The argon/oxygen (Ar/O_2) flow rates, sputtering pressure, RF power, substrate temperature, and process time were set to 30 sccm/3 sccm, 5 mTorr, 50 W, 20 ºC, and 10 min, respectively. The thickness of the deposited In_2O_3 film is ~13 nm. After the sputtering, the post-deposition annealing (PDA) was finally performed to crystallize the In_2O_3 film in a vacuum at 300 ºC for 10 min.

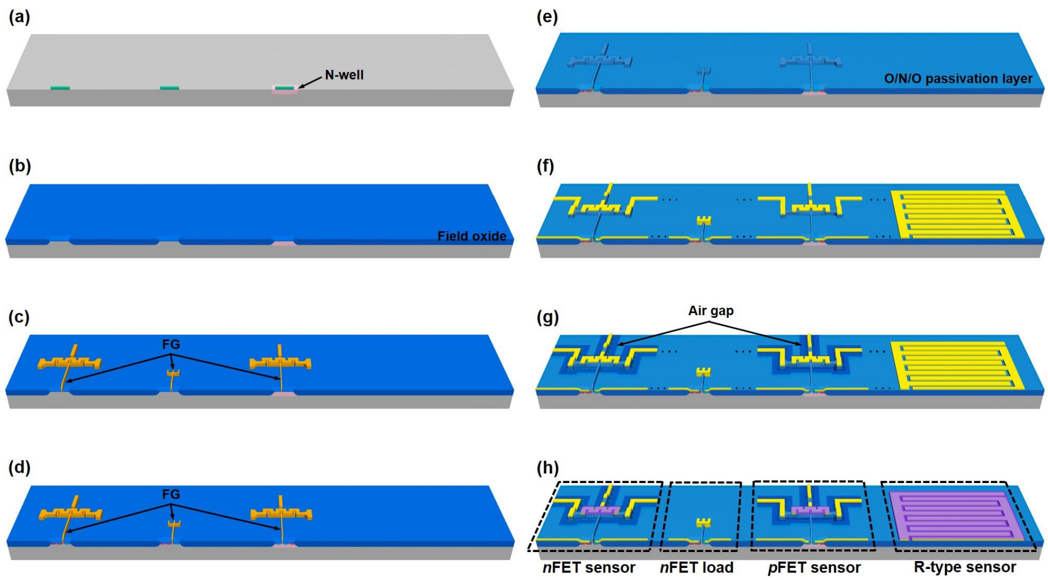

Fig. 2.5. (a)-(f) Cross sectional view of the fabrication process of the Si CMOS-based interface circuit with gas sensors.

Chapter 3

Characteristics of amplifier circuits

3.1 Electrical and sensing characteristics of unit sensors

In this dissertation, the *n*FET- and *p*FET-type gas sensors and *n*- and *p*-channel FETs of the amplifier circuits were fabricated on the same substrate. The electrical characteristics of the FET-type gas sensors and FET elements are analyzed using a semiconductor parameter analyzer (B1500A, Agilent). Fig. 3.1(a) and (b) show the transfer (I_D-V_{CG}) curves of the *n*FET- and *p*FET-type gas sensors as a parameter of the operating temperature (20 ºC ~ 160 ºC). As the operating temperature increases, the off current (I_{off}) increases since a leakage current increases at the junction of the source/drain and the substrate at higher operating temperatures [44]. Fig. 3.2(a) and (b) show the transfer curves of the load FETs and FET-type gas sensors with *n*- and *p*-channel at 20 ºC and 160 ºC. The *W*/*L*s of the *n*FET- and *p*FET-type gas sensors are 1 μm/1 μm. And the *W*/*L*s of the load FETs with *n*- and *p*-channel are 1 μm/4 μm. The fabricated FET devices have flash memory functionality because of their CG and FG. Fig. 3.3(a) and (b) show the flash memory functionality of the FET-type gas sensors and FET elements under the different program voltage (V_{PGM}) and erase voltage (V_{ERS}) at 20 °C. The V_{PGM} or V_{ERS} was applied to the CG for 5 sec, and the body, source, and drain of the flash memories were grounded simultaneously. When the positive V_{PGM} is applied to the CG, the transfer curve of the *n*FET and *n*FET-type gas sensor moves to the positive bias direction. On the other hand, the transfer curve of the *n*FET devices moves to the negative bias direction by the negative V_{ERS} (Fig. 3.3(a)). Fig. 3.3(b) shows the flash memory functionality of the *p*FET and *p*FET-type gas sensor. The bias condition for the program/erase in the *p*FET devices is opposite to that in the *n*FET devices. The tunable V_{th} of the FET elements facilitates the calibration of sensor signals and adjustment of the operating point of the FET elements in a read-out circuitry, such as a transimpedance amplifier (TIA). The resistor-type gas sensor was also fabricated on the same substrate with the FETs and FET-type gas sensors. Fig. 3.4 shows *I*-*V* curve of the resistor-type gas sensor at 20 °C and 160 °C.

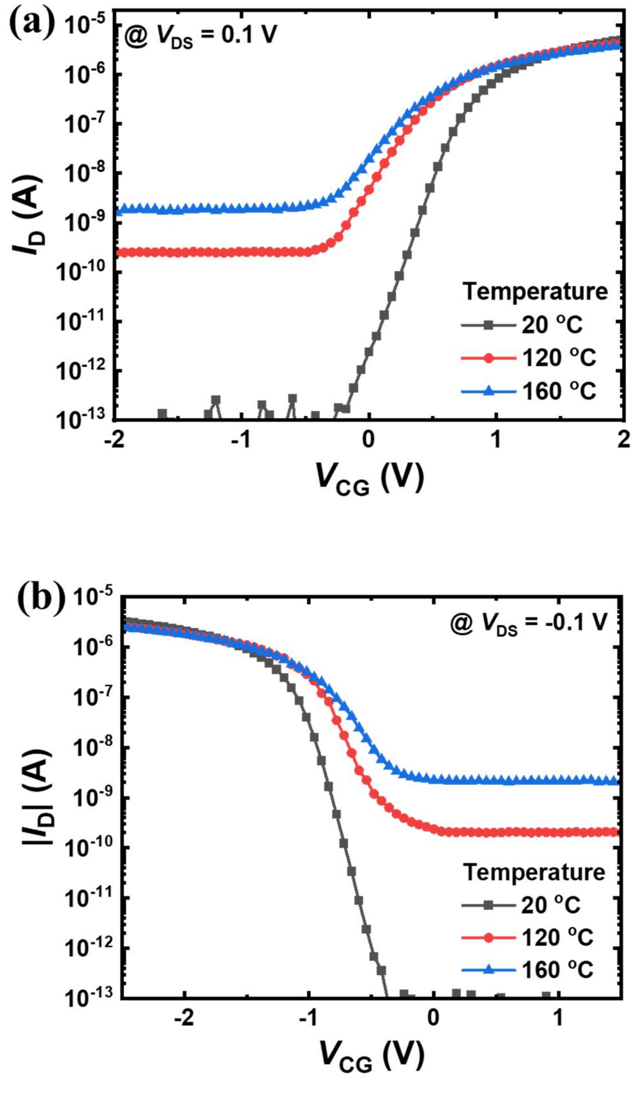

Fig. 3.1. I_D-V_{CG} curves of the fabricated (a) *n*FET-type and (b) *p*FET-type gas sensor as a parameter of the operating temperature (20 ºC ~160 ºC).

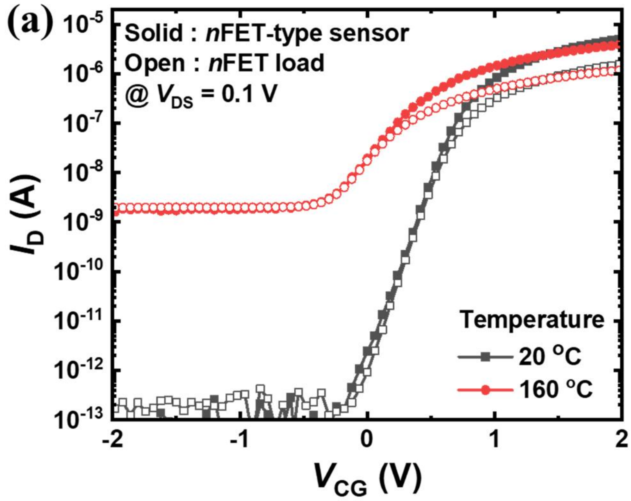

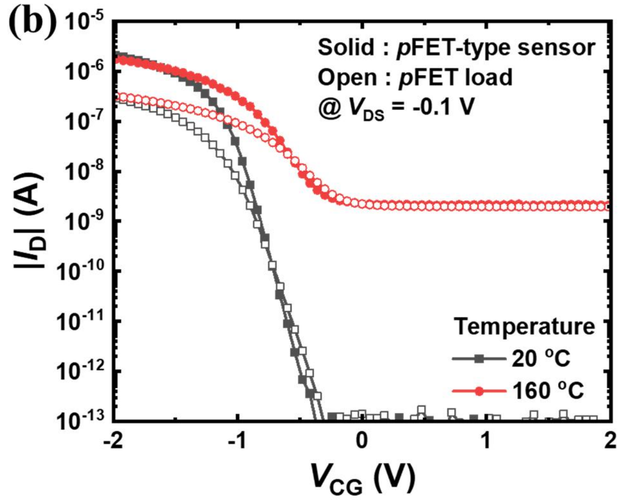

Fig. 3.2. I_D-V_{CG} curves of the fabricated (a) *n*FET and *n*FET-type gas sensor and (b) *p*FET and *p*FET-type gas sensor at 20 ºC and 160 ºC.

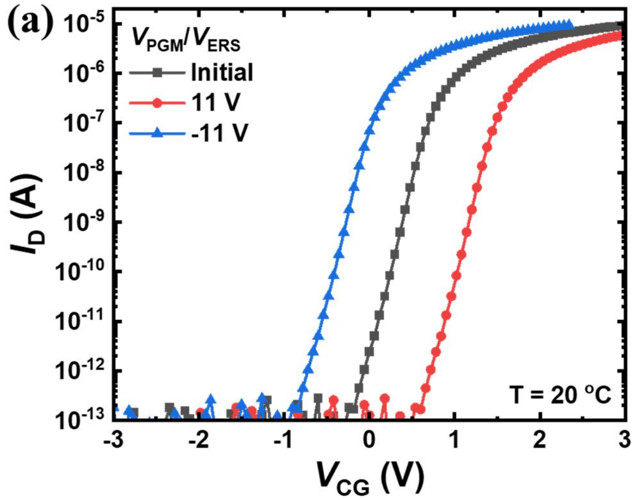

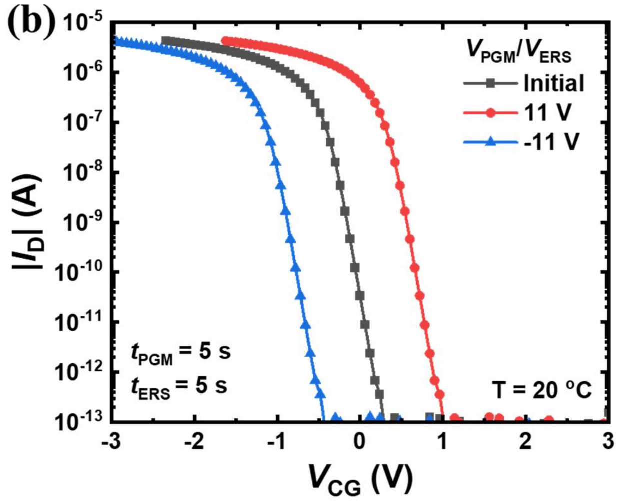

Fig. 3.3. Program/Erase characteristics of the (a) *n*FET- and (b) *p*FET-type gas sensors under the different V_{PGM} and V_{ERS} at 20 ºC.

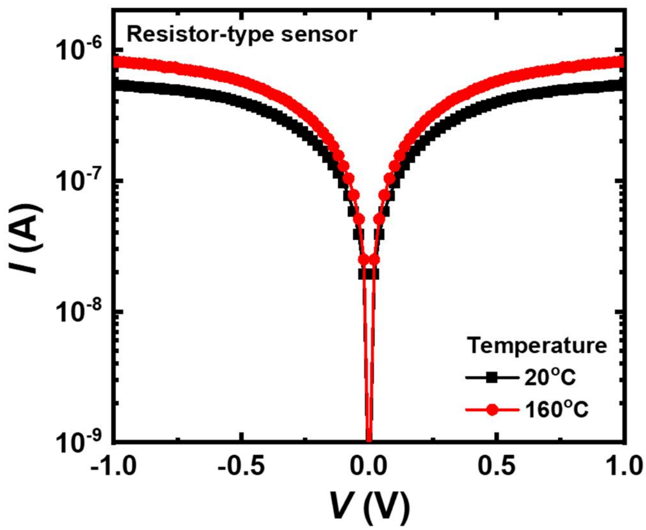

Fig. 3.4. *I*-*V* characteristics of the fabricated resistor-type gas sensor with In_2O_3 sensing layer at 20 ºC and 160 ºC.

Fig. 3.5 shows the energy band diagram of the *p*FET-type gas sensor in the atmosphere of dry air and NO_2 gas. Fig. 3.6(a) and (b) show the transient ID behaviors of the *n*FET- and *p*FET-type gas sensors according to the NO_2 gas concentration. When the gas sensors are exposed to the NO_2 gas, the NO_2 gas is adsorbed on the *n*-type In_2O_3 sensing layer and steals electrons from the sensing layer as an oxidizing gas [45]. The adsorbed NO_2 gas molecules are ionized at the interface between the In_2O_3 sensing layer and the O/N/O passivation layer. At this interface, the ionized gas molecules deplete the sensing layer and function as an effective negative charge [46]. The threshold voltage (V_{th}) of the FET-type gas sensor moves to the positive bias direction as a result of this negative charge inducing a positive charge in the FET channel. Therefore, as shown in Fig. 3.6(a) and (b), the drain current of the *n*FET- and *p*FET-type sensor decreases and increases when exposed to the NO_2 gas, respectively. The transient I_D behavior of the resistor-type gas sensor at 160 °C according to the NO_2 concentration. As mentioned above, the resistance of the In2O3 sensing material partially depleted by the negatively ionized NO_2 gas molecules increases, and then, the current of the resistor-type sensor decreases. Fig. 3.8 shows the response of *n*FET- and *p*FET-type gas sensors and the resistor-type gas sensor to NO_2 concentration. The response of these gas sensors is nonlinear and follows Langmuir's theory [47].

On the other hand, H_2S gas molecules are known as reducing gas [48]. As a reducing gas, the H_2S gas molecules donate electrons to the In_2O_3 sensing layer. At the interface between the sensing layer and passivation layer, ionized H_2S gas molecules induce a negative charge in the FET channel by acting as an effective positive charge. Thus, the V_{th} of the FET-type gas sensor moves to the negative bias direction. As shown in Fig. 3.9(a) and (b), the drain current increases in the *n*FET-type sensor and decreases in the *p*FET-type sensor, as opposed to the NO_2 gas, when exposed to the H_2S gas. As opposed to the NO_2 gas, H_2S gas molecules reduce the depletion region of the *n*-type In_2O_3 sensing layer. Thus, the resistance of the resistor-type sensor decreases, and then, the current of the resistor-type sensor increases when exposed to the H_2S gas, as shown in Fig. 3.10.

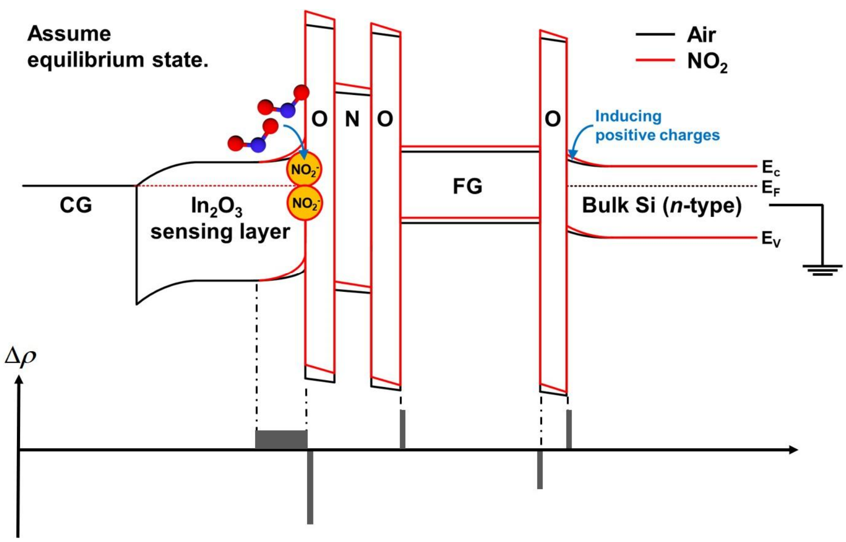

Fig. 3.5. Energy band diagram of the fabricated FET-type gas sensor when exposed to air and NO_2 gas ambience. $\Delta\rho$ is additionally introduced below.

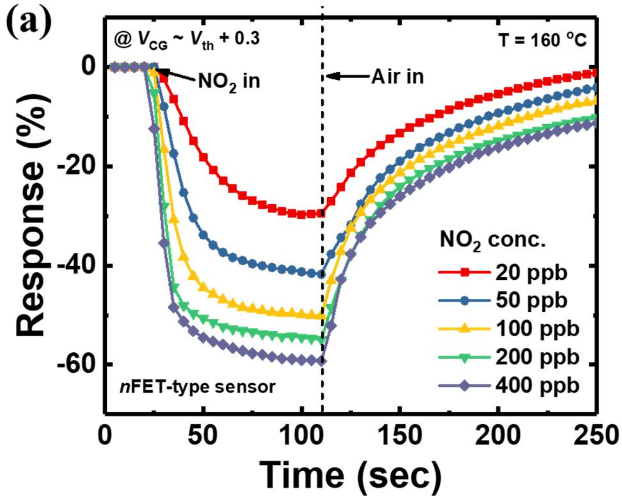

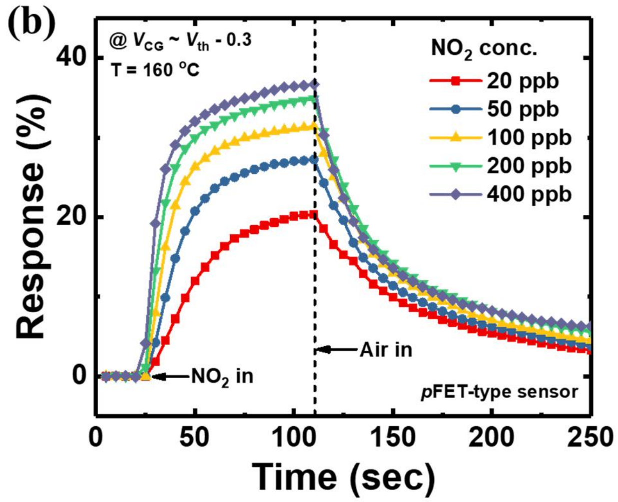

Fig. 3.6. Transient sensing characteristics of the (a) *n*FET-type and (b) *p*FET-type gas sensor as a parameter of NO_2 gas concentration (0 ppb ~ 400 ppb) at 160 ºC. Here, $V_{CG} = V_{th} \pm 0.3$ V and $V_{DS} = \pm 0.1$ V.

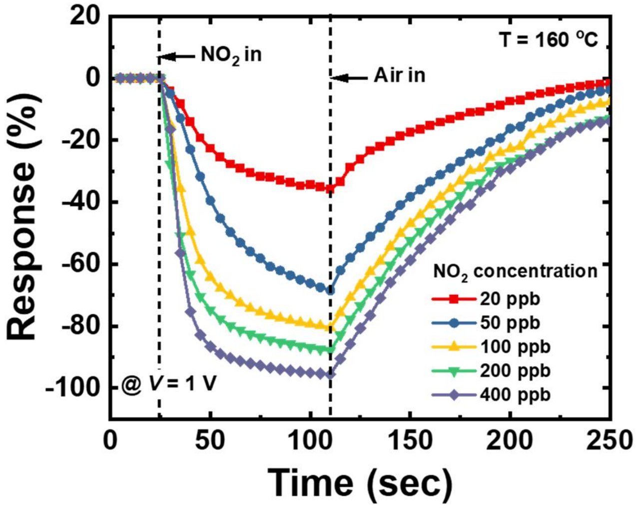

Fig. 3.7. Transient sensing characteristics of the resistor-type gas sensor as a parameter of NO_2 gas concentration (0 ppb ~ 400 ppb) at 160 °C.

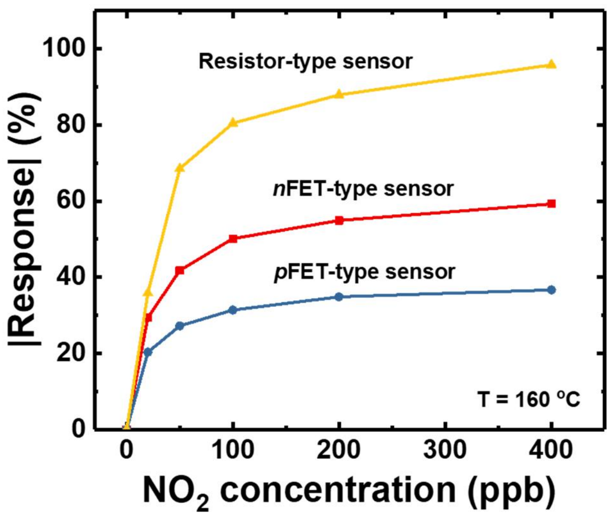

Fig. 3.8. Response of *n*FET-type and *p*FET-type gas sensors and a resistor-type gas sensor versus NO_2 concentration. All responses follow Langmuir theory.

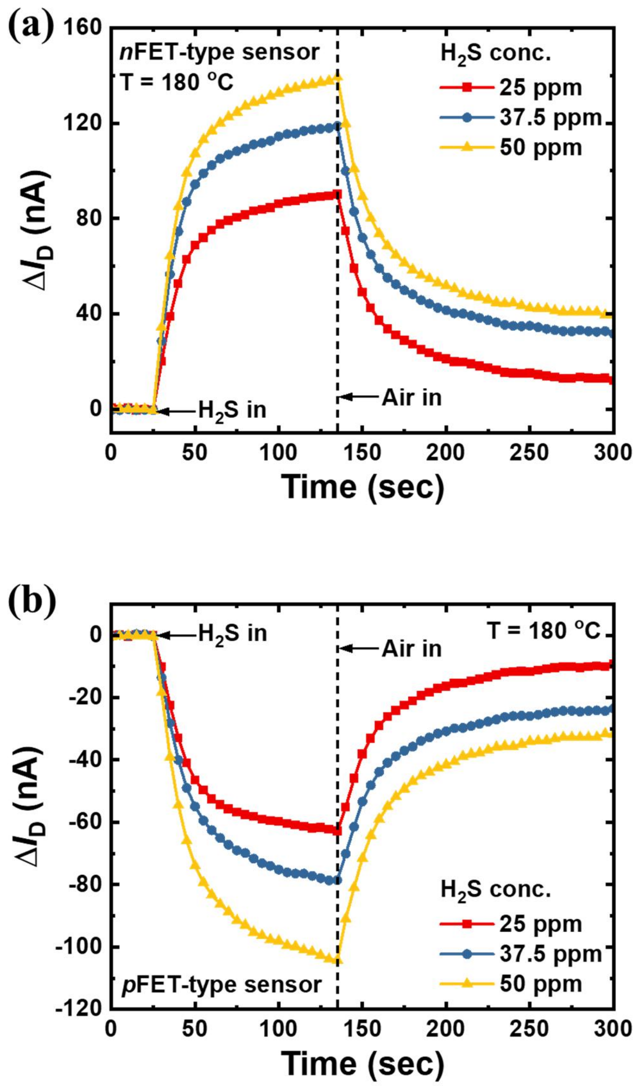

Fig. 3.9. Transient sensing characteristics of the (a) *n*FET-type and (b) *p*FET-type gas sensor as a parameter of H_2S gas concentration (25 ppm ~ 50 ppm) at 180 ºC.

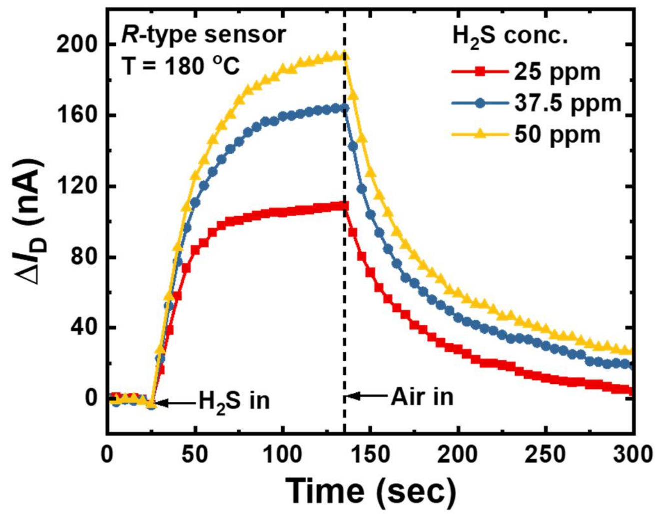

Fig. 3.10. Transient sensing characteristics of the resistor-type gas sensor as a parameter of H_2S gas concentration (25 ppm ~ 50 ppm) at 180 ºC.

3.2 Electrical characteristics of amplifier circuits

In this dissertation, the electrical and sensing characteristics of four different amplifier circuits are proposed and analyzed. The four different circuits in this dissertation are *n*- and *p*-type amplifier circuits with FET loads and *n*- and *p*-type amplifier circuits with resistor-type (R-type) sensors. First, an *n*-type amplifier circuit with FET load is composed of the *n*FET-type gas sensor with load FET with *n*-channel. Fig. 3.11(a) shows the transfer curve (V_{out}-V_{in}) of the *n*-type amplifier circuit with FET load. As shown in Fig. 3.11(a), the transfer curve is changed according to the bias voltage applied to the CG of the FET load (V_b) since the electrical characteristics of the FET load with different V_b. Fig. 3.11(b) shows the gain (= V_{out}/V_{in}) of the *n*-type amplifier circuit with FET load versus V_{in} as a parameter of V_b. The voltage gain curve of the amplifier circuit versus V_{in} has a maximum at a specific V_{in}. In addition, the amplifier circuit has the highest maximum gain at $V_b = 0.8$ V and $V_{in} = 0.12$ V since the amplifier gain is influenced by V_b. Fig. 3.12(a) shows the V_{out}-V_{in} curves of the *p*-type amplifier circuit with FET load consisting of the *p*FET-type gas sensor with *p*FET load. As shown in Fig.

3.12(a), the transfer curve is also changed according to the V_b. Fig. 3.12(b) shows the gain (= V_{out}/V_{in}) of the *p*-type amplifier circuit with FET load versus V_{in} as a parameter of V_b. The *p*-type amplifier circuit with FET load has the highest maximum gain at V_b = -1.0 V and V_{in} = -0.26 V. Since the voltage gain of the amplifier circuit affects the sensitivity in the response, the sensing characteristics are analyzed at the V_b where the voltage gain is maximum. Fig. 3.13(a) shows the V_{out}-V_{in} and voltage gain of the *n*-type amplifier circuit with a resistor-type sensor. The amplifier circuit consists of the *n*FET- and the resistor-type sensors. The maximum voltage gain of the *n*-type amplifier circuit with the resistor-type sensor is approximately 4.78 V/V at V_{in} = 0.12 V. Fig. 3.13(b) shows the V_{out}-V_{in} and voltage gain of the amplifier circuit consisting of the *p*FET- and the resistor-type sensors. The maximum voltage gain of the *p*-type amplifier circuit with the resistor-type sensor is 4.82 V/V at V_{in} = 0.24 V, which is almost similar to the gain of the *n*-type amplifier circuit with the resistor-type sensor.

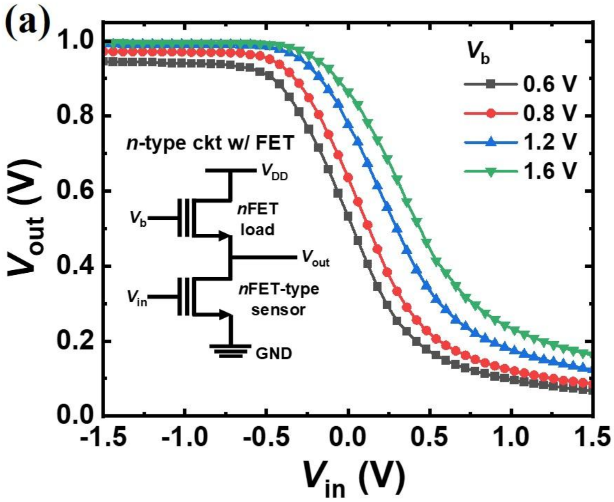

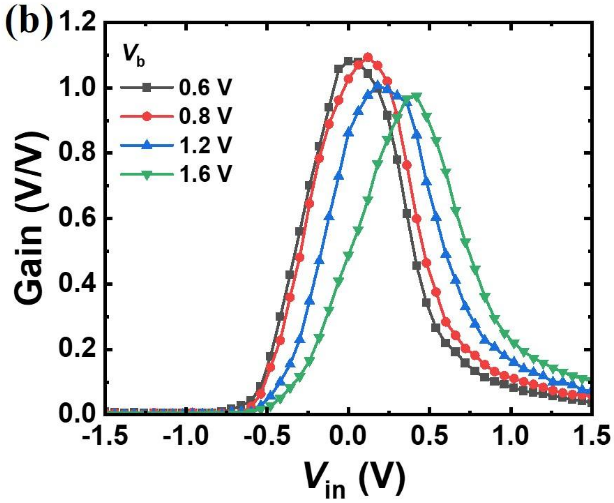

Fig. 3.11. (a) Transfer curves (V_{out}-V_{in}) and (b) voltage gain (= V_{out}/V_{in}) of the *n*-type amplifier circuit with FET load as a parameter of V_b (0.6 V ~ 1.6 V). The V_b is a bias voltage applied to the CG of the *n*FET load. At V_b = 0.8 V and V_{in} = 0.12 V, the amplifier circuit has maximum gain.

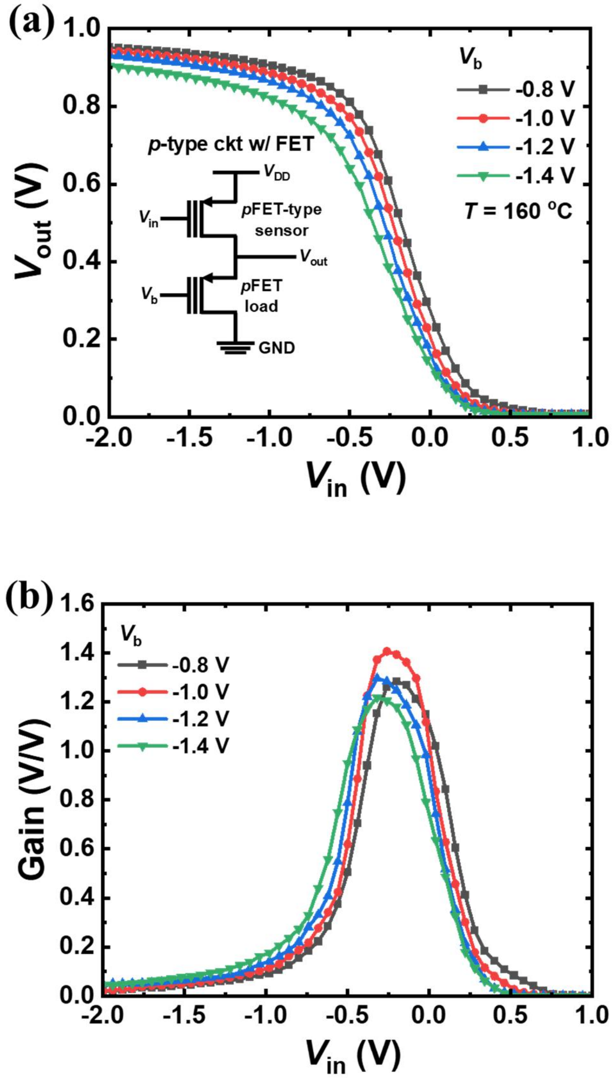

Fig. 3.12. (a) Transfer curves (V_{out}-V_{in}) and (b) voltage gain (= V_{out}/V_{in}) of the p-type amplifier circuit with FET load as a parameter of V_b (-0.8 V ~ -1.4 V). The V_b is a bias voltage applied to the CG of the pFET load. At V_b = -1.0 V and V_{in} = -0.26 V, the amplifier circuit has maximum gain.

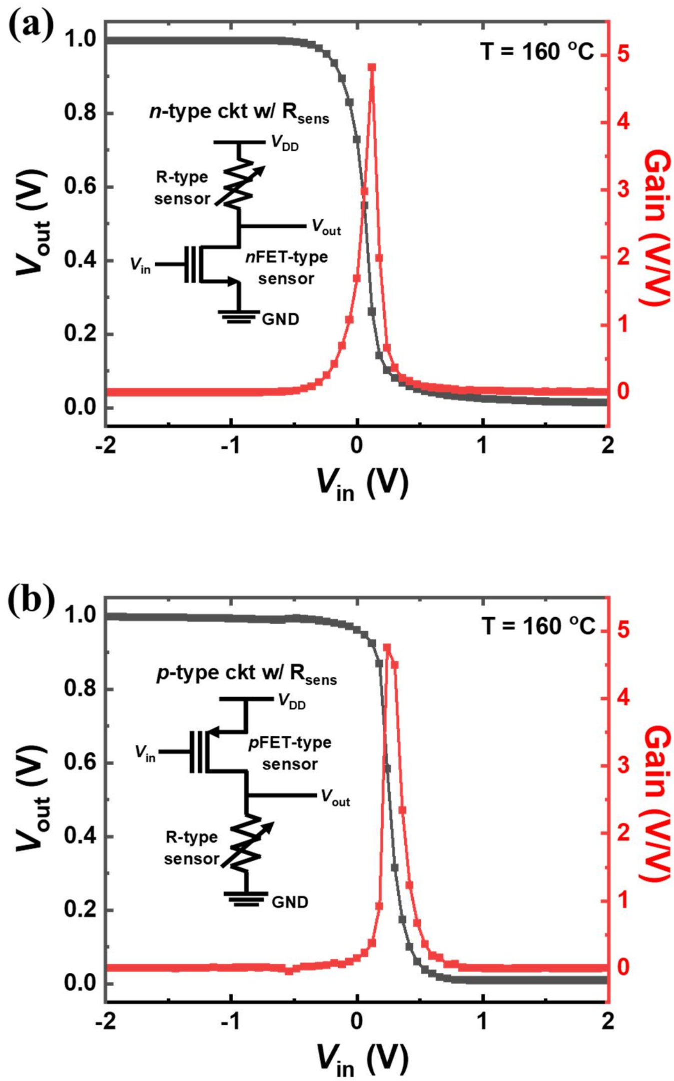

Fig. 3.13. Transfer curves (V_{out}-V_{in}) and voltage gain (= $V_{\text{out}}/V_{\text{in}}$) of (a) the *n*-type amplifier circuit with R-type sensor and (b) the *p*-type amplifier circuit with R-type sensor at 160 ºC. The maximum voltage gain of the *n*- and *p*-type amplifier circuits are 4.78 V/V at V_{in} = 0.12 V and 4.82 V/V at V_{in} = 0.24 V, respectively.

3.3 Sensing characteristics of amplifier circuits

Fig. 3.14(a) shows the transfer curves of the *n*-type amplifier circuit with FET load according to the NO_2 concentration. Insets in Fig. 3.14(a) show the configuration of the amplifier circuit. Since the V_{th} of the *n*FET-type sensor moves to the positive bias direction by reaction with the NO_2 gas, the drain current of the sensor decreases. Thus, the voltage across the *n*-type FET load decreases and the V_{out} of the circuit increases to reduce the current flowing through the circuit. Fig. 3.14(b) shows $V_{out,gas}$-$V_{out,air}$ (~ΔV_{out}) versus V_{in} obtained from the transfer curves in Fig. 3.14(a). When exposed to 500ppb of NO_2 gas, the maximum $|\Delta V_{out}|$ is approximately 220 mV. In here, $V_{out,air}$ and $V_{out,gas}$ are the output voltage of the amplifier circuit in air and gas ambience, respectively. Fig. 3.15(a) shows the transfer curves of the *p*-type amplifier circuit with FET load according to the NO_2 concentration. Insets in Fig. 3.15(a) show the amplifier circuit configuration. The drain current of the *p*FET-type sensor increases as the NO_2 gas concentration increases. Therefore, the voltage across the *p*-type FET load and the V_{out} increases to increase the current flowing through the circuit. Fig. 3.15(b) shows ΔV_{out} of the amplifier circuit versus V_{in}, in which the maximum $|\Delta V_{out}|$ is approximately 200 mV. Fig. 3.16(a) and (b) show the $|\Delta V_{out}|$ of the *n*- and *p*-type amplifier circuits with FET loads versus NO_2 concentration as a parameter of V_{in}. In the transition region of the amplifier circuits, the *n*FET- and *p*FET-type sensors operate as a current source since the FET-type sensors operate in the saturation region. And the FET loads have a fixed resistance. Therefore, $|\Delta V_{out}|$ of the amplifier circuits follows Langmuir's theory, like a current change of the FET-type sensor.

Fig. 3.17(a) shows the transfer curves (V_{out}-V_{in}) of the *n*-type amplifier circuit with a resistor-type sensor as a parameter of NO_2 concentration. The current in *n*FET- and resistor-type gas sensors decreases by reaction with the NO_2 gas molecules. Since the *n*FET-type sensor operates in the saturation region, its current is unaffected by V_{out}, and the current flowing through the circuit is determined by the *n*FET-type gas sensor. And, the current of these two sensors in the circuit should be the same since the *n*FET- and resistor-type gas sensor is connected into a series. But, the response of the resistor-type gas sensor is larger than that of the *n*FET-type gas sensor. To compensate difference of the sensitivity, the voltage across the resistor-type sensor increases. Therefore, V_{out} of the circuit should be decreased as NO_2 gas concentration increases. Fig. 3.17(b) shows the $|\Delta V_{out}|$ versus V_{in} of the n-type amplifier circuit with FET load as a parameter of NO_2 gas concentration. When exposed to 500 ppb of NO_2 gas, the maximum $|\Delta V_{out}|$ is approximately 827 mV.

Fig. 3.18(a) shows the transfer curves of the p-type amplifier circuit with resistor-type sensor as a parameter of NO_2 gas concentration. The current of the pFET-type and resistor-type sensors in the amplifier circuit will try to increase and decrease, respectively, by reaction with the NO_2 gas molecules. The current flowing in the amplifier circuit increases since the current is determined by the pFET-type sensor, which is operating in the saturation region. But, the resistance of the resistor-type sensor increases in the NO_2 gas response. Therefore, compared to the other amplifier circuit, the voltage across the resistor-type sensor increases ($\sim V_{out}$ increase) more significantly in this circuit. The complementary sensing characteristics of the pFET- and resistor-type sensor improve the sensitivity of the p-type amplifier circuit with resistor-type sensor. Fig. 3.18(b) shows the $|\Delta V_{out}|$ versus V_{in} of the p-type amplifier circuit with resistor-type sensor as a parameter of NO_2 gas concentration.

When exposed to 500 ppb of NO_2 gas, the maximum $|\Delta V_{out}|$ is 947mV, which is relatively large compared to other amplifier circuits.

Fig. 3.19(a) and (b) show $|\Delta V_{out}|$ of the *n*-type and *p*-type amplifier circuits with resistor-type sensors versus NO_2 concentration as a parameter of V_{in}. At a specific input voltage, $|\Delta V_{out}|$ increases almost linearly as NO_2 concentration increases. This linear sensitivity allows the amplifier circuit to detect a wide range of gas concentrations. Also, it simplifies the peripheral circuit, which is very useful for reducing power consumption. As shown in Fig. 3.19(a), the $|\Delta V_{out}|$ of the *n*-type amplifier circuit with resistor-type sensor versus NO_2 concentration at V_{in}= -0.42 V is close to linear (R^2= 0.989) and its slope is 0.582 mV/ppb. In Fig. 3.19(b), the *p*-type amplifier circuit with resistor-type sensor has a good linearity (R^2= 0.985) and a higher sensitivity of 2.2 mV/ppb at a V_{in}= 0.66 V. It also can detect low concentration gas with an even higher sensitivity of 8.96 mV/ppb at V_{in}= 0.6 V.

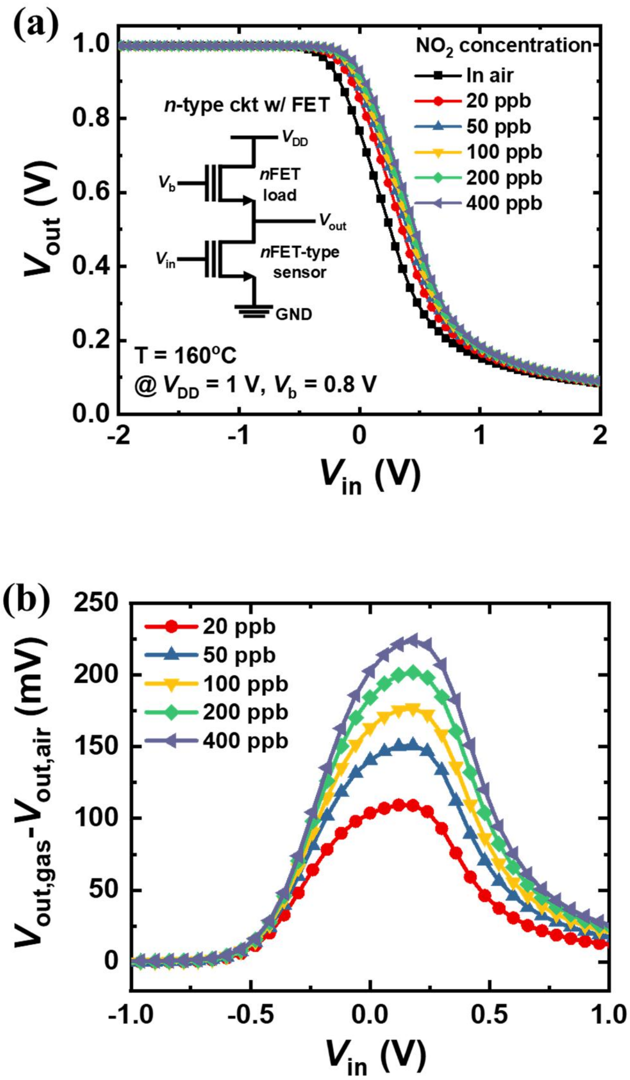

Fig. 3.14. (a) Transfer curves of the amplifier circuit consisting of an *n*FET-type gas sensor and an *n*FET load as a parameter of NO_2 concentration. The inset shows the circuit diagram of the amplifier circuit. (b) $V_{out,gas}$ - $V_{out,air}$ of the *n*-type amplifier circuit with FET load versus V_{in} as a parameter of NO_2 concentration.

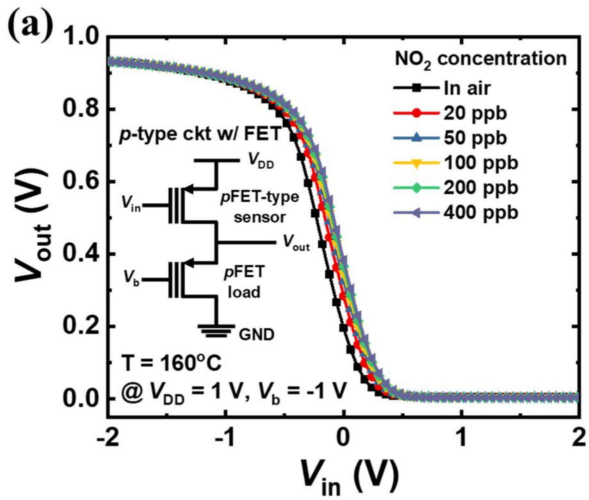

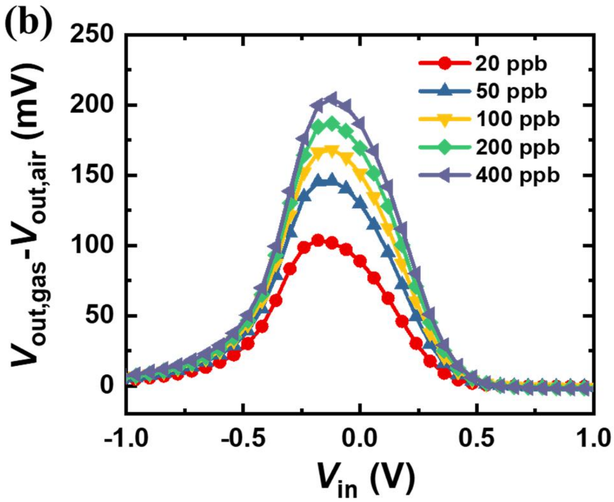

Fig. 3.15. (a) Transfer curves of the amplifier circuit consisting of a *p*FET-type gas sensor and a *p*FET load as a parameter of NO_2 concentration. The inset shows the circuit diagram of the amplifier circuit. (b) $V_{out,gas}$ - $V_{out,air}$ of the *p*-type amplifier circuit with FET load versus V_{in} as a parameter of NO_2 concentration.

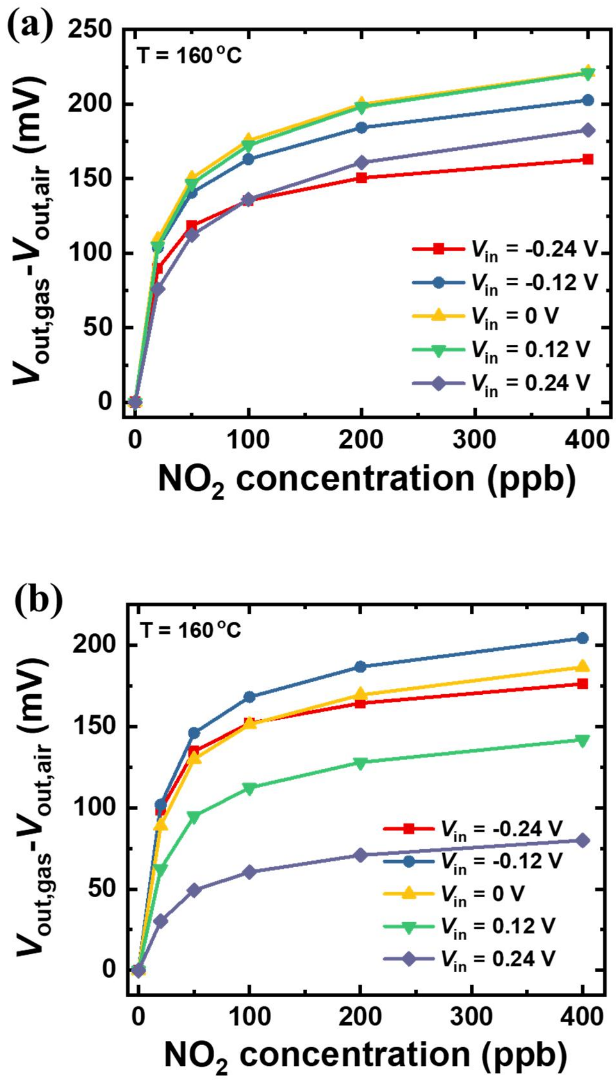

Fig. 3.16. $V_{out,gas}$ - $V_{out,air}$ of the (a) *n*-type amplifier circuit and (b) *p*-type amplifier circuit with FET load versus NO_2 concentration as a parameter of V_{in}. The curves in these figures follow the Langmuir's theory.

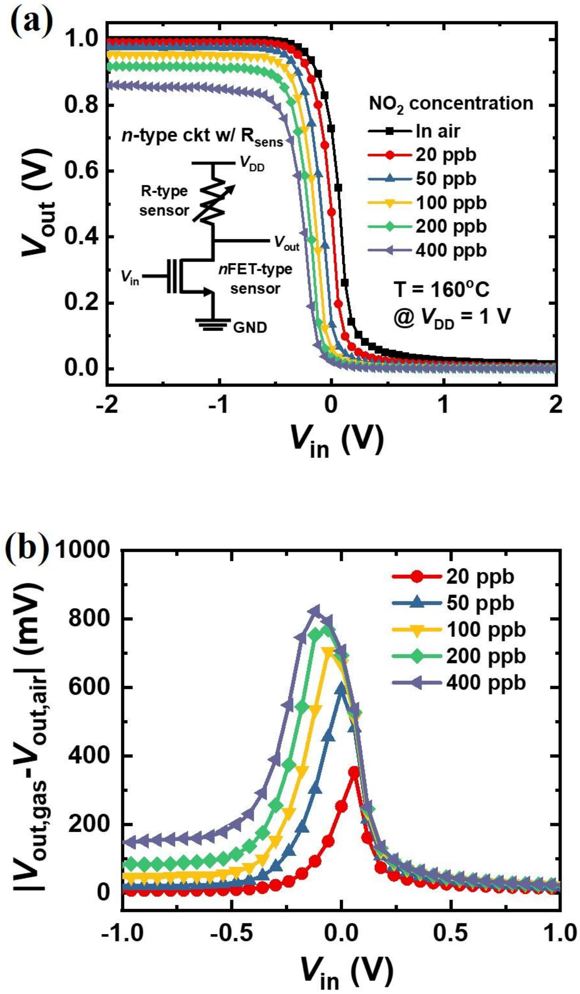

Fig. 3.17. (a) Transfer curves of the amplifier circuit consisting of the *n*FET- and resistor-type gas sensors as a parameter of NO_2 concentration. The currents of both sensors in the amplifier circuit change in same direction by the NO_2 gas reaction. (b) $V_{out,gas}$ - $V_{out,air}$ of the *n*-type amplifier circuit with resistor-type sensor versus V_{in} as a parameter of NO_2 concentration.

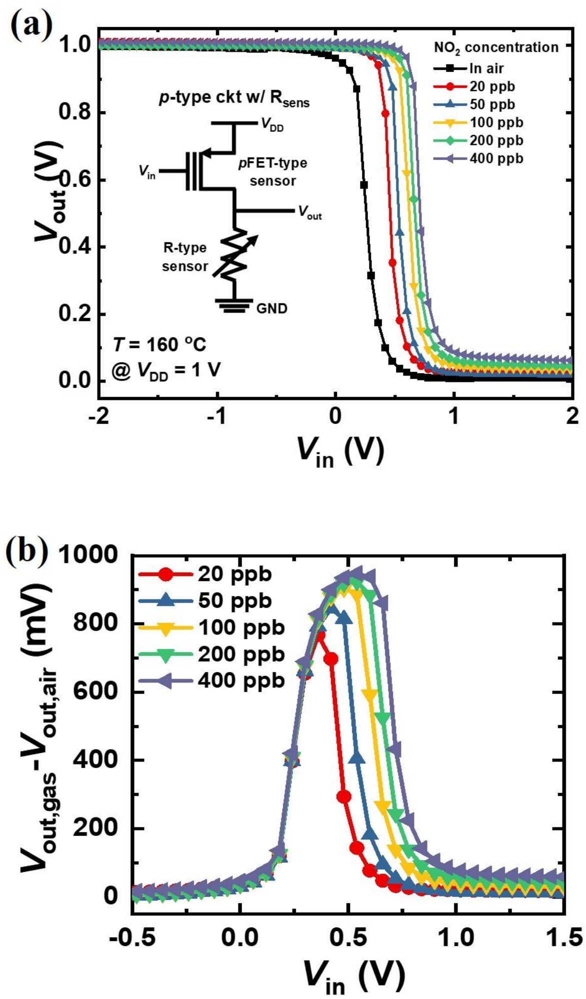

Fig. 3.18. (a) Transfer curves of the amplifier circuit consisting of the *p*FET- and resistor-type gas sensors as a parameter of NO_2 concentration. The currents of both sensors in the amplifier circuit change in opposite directions by the NO_2 gas reaction. (b) $V_{out,gas}$ - $V_{out,air}$ of the *p*-type amplifier circuit with resistor-type sensor versus V_{in} as a parameter of NO_2 concentration.

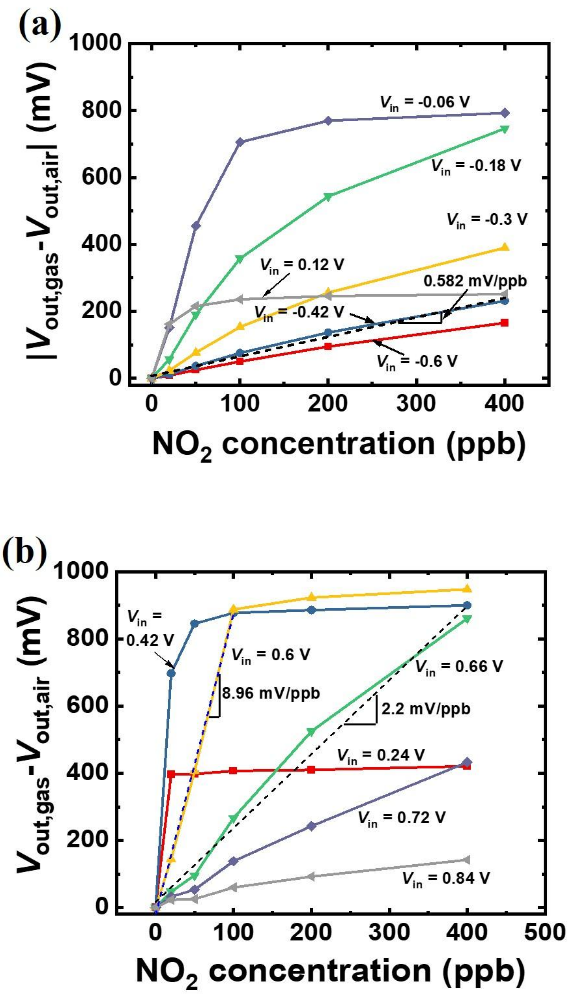

Fig. 3.19. $V_{\mathrm{out,gas}}$ - $V_{\mathrm{out,air}}$ of (a) the *n*-type and (b) *p*-type amplifier circuit with R-type sensors versus NO_2 concentration. The $|V_{\mathrm{out,gas}}$ - $V_{\mathrm{out,air}}|$ versus NO_2 concentration in the *n*-type circuit is close to linear (R^2= 0.989) at V_{in} = -0.42 V and its slope is 0.582 mV/ppb. The $V_{\mathrm{out,gas}}$ - $V_{\mathrm{out,air}}$ in the *p*-type circuit is close to linear (R^2= 0.985) at V_{in} = 0.66 V and its slope is 2.2 mV/ppb.

3.4 Low frequency noise characteristics of amplifier circuits

The normalized current noise power spectral density (S_I/I^2) of the resistor-type gas sensor and n$^+$ doped poly-Si resistor is shown in Fig. 3.20(a). The poly-Si resistor exhibits very little thermal noise, whereas the resistor-type sensor shows considerable low frequency (1/f) noise because the carrier mobility varies greatly at the In_2O_3 thin-film grain boundaries. Also, the current noise power spectral density (S_I) of the resistor-type sensor is unaffected by the voltage across the sensor (Fig. 3.20(b)). The normalized drain current noise power spectral density (S_{ID}/I_D^2) of the *n*FET- and the *p*FET-type gas sensors is investigated (Fig. 3.21(a)). Fig. 3.21(b) shows the log-log plot of S_{ID}/I_D^2s of the FET-type sensors sampled at 10 Hz versus I_D. The physical origin of the low frequency noise in the *n*FET-type gas sensors is verified by the carrier number fluctuation (CNF). The CNF model is represented as [49]:

$$\frac{S_{ID}}{{I_D}^2} = \left(\frac{g_m}{I_D}\right)^2 \frac{q^2 KT N_T \lambda}{WL{C_{ox}}^2 f}, \tag{1}$$

where N_T is volume trap density, λ is the tunneling attenuation coefficient in the gate oxide, and C_{ox} is the gate oxide capacitance per unit area. The S_{ID}/I_D^2 of the

nFET-type sensor with respect to I_D exhibits the same characteristics as $(g_m/I_D)2$, as illustrated in Fig. 3.21(b), demonstrating that the CNF is the physical origin of the $1/f$ noise. As shown in Fig. 3.21(b), S_{ID}/I_D^2 has a slight deviation from $(g_m/I_D)^2$, which is due to the existence of correlated mobility fluctuation [50].

The physical origin of the low frequency noise in the pFET-type gas sensor is verified by Hooge's mobility fluctuation (HMF). The HMF model is represented as [51]:

$$\frac{S_{ID}}{{I_D}^2} = \frac{\alpha_H {\mu_{eff}}^2 kT}{f L^2 I_D} \qquad (2)$$

where μ_{eff} is the effective carrier mobility. The S_{ID}/I_D^2 of the pFET-type sensor with regard to I_D is proportional to I_D^{-1} demonstrating that the $1/f$ noise originated from the HMF (Fig. 3.21(b)). The $1/f$ noise of the nFET-type sensor shows about ten times more than that of the pFET-type sensor since the $1/f$ noise of the nFET-type sensor is originated from the CNF at the Si-SiO_2 interface, whereas that of the pFET-type sensor is originated from the HMF in the Si bulk. Since the signal-to-noise ratio (SNR) of a gas sensor determines the signal resolution and the limit of detection (LOD), it is important to investigate the SNR of a gas sensor to optimize sensing performance. Also, the SNR of the amplifier circuit consisting of the gas sensors should be investigated. The SNR of the amplifier circuit is defined as

$$\mathrm{SNR} = \frac{|\Delta V_{out}|}{\delta V_{out}} = \frac{|V_{out,gas} - V_{out,air}|}{\sqrt{\int_{f_1}^{f_2} S_{Vout} df}} \quad (3)$$

where δV_{out} is the root-mean-square output voltage noise amplitude, S_{Vout} is the power spectral density of output voltage, and f_1 and f_2 correspond to low- and high-frequency cutoff, respectively. Since the noise sources of the devices constituting the amplifier circuit are uncorrelated, the S_{Vout} of the amplifier circuit is derived by adding the voltage noise power of the FET-type gas sensor and load (FET load or resistor-type sensor). The voltage noise power of the devices can be calculated by adding current noise power divided by the square of the corresponding output conductance in each element [52]. It is important to note that S_{Vout} cannot be determined simply by dividing the load current noise by the square of the inverter output conductance (g_{out}). The $|\Delta V_{\mathrm{out}}|$ and S_{Vout} as a function of V_{in} of the *n*-type and *p*-type amplifier circuits with FET loads are investigated as shown in Fig. 3.22(a) and (b), respectively. The S_{Vout} of the amplifier circuit consisting of the FET-type sensor and FET load is expressed as

$$S_{Vout} = S_{V,sensor} + S_{V,load} = \frac{S_{ID,sensor}}{{g_{d,sensor}}^2} + \frac{S_{ID,load}}{{g_{d,load}}^2} \quad (4)$$

where $S_{V,sensor}$ and $S_{V,load}$ are the voltage noise power of the FET-type gas sensor and FET load, and $g_{d,sensor}$ and $g_{d,load}$ are the output conductance of the FET-type gas sensor and FET load. The S_{Vout} of the n-type amplifier circuit with FET load is not changed depending on V_{in} as shown in Fig. 3.22(a). On the other hand, the g_m is the highest at V_{in} near 0 V, where the S_{Vout} of the p-type amplifier circuit with FET load is the smallest (Fig. 3.22(b)). The $|\Delta V_{out}|$ and S_{Vout} as a function of V_{in} of the n-type and p-type amplifier circuits with the resistor-type sensors are shown in Fig. 3.23(a) and (b). The S_{Vout} of the amplifier circuit consisting of the FET- and resistor-type sensor is expressed as

$$S_{Vout} = S_{V,R} + S_{V,FET} = {R_{In2O3}}^2 S_I + \frac{S_{ID}}{{g_d}^2} \quad (5)$$

where $S_{V,R}$ and $S_{V,FET}$ are the voltage noise power of the resistor- and FET-type gas sensors and g_d is the output conductance of the FET-type gas sensor. Since the current flowing through the resistor-type sensor increase while the R_{In2O3} remains constant, the $S_{V,R}$ increases as V_{in} increases. As shown in Fig. 3.23(b), the S_{Vout} is determined by the LFN of the resistor-type gas sensor. The S_{Vout} of the amplifier circuit is defined by the sensor with the higher voltage noise since the noise sources of the FET- and resistor-type gas sensors are uncorrelated. Compared to the FET-type sensor, whose conductance is determined by crystalline Si, the resistor-type sensor shows large $1/f$ noise because its low frequency noise is determined by polycrystalline In_2O_3. The SNRs as a function of V_{in} of four different amplifier circuits are compared (Fig. 3.24). The SNRs of the amplifier circuits are obtained by dividing the $|\Delta V_{out}|$ with the square root of S_{Vout}. As the S_{Vout} is constant regardless of V_{in}, the behavior of SNR in the n-type amplifier circuit with FET load follows the behavior of the $|\Delta V_{out}|$. At V_{in} around 0 V, where g_m is the largest, the SNR of the p-type amplifier circuit with FET load is largest. On the other hand, the SNRs of the n-type and p-type amplifier circuits with resistor-type sensors are mainly determined by the noise behavior of the resistor-type sensor. As a result, the SNR of the amplifier circuits with the resistor-type sensor is the largest when the noise of the resistor-type sensor is the smallest. The p-type amplifier circuit with the resistor-type sensor has an excellent SNR of 10^3 at V_{in} in the range of 0.6 V to 0.66 V with good linearity (R^2>0.98) and high sensitivity up to 8.96 mV/ppb.

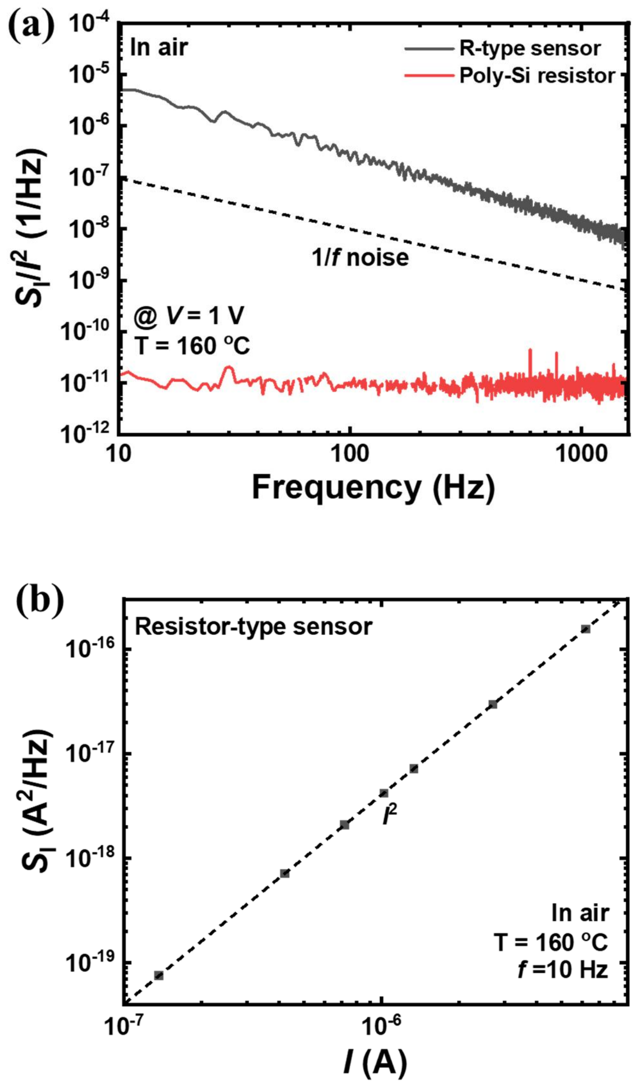

Fig. 3.20. (a) Normalized current noise power spectral densities (S_I/I^2s) of resistor-type sensor and n^+ poly-Si resistor measured at 160 °C. The resistor-type sensor with an In_2O_3 sensing material exhibits 1/*f* noise behavior. (b) The log-log plot of S_I sampled at 10 Hz versus *I*.

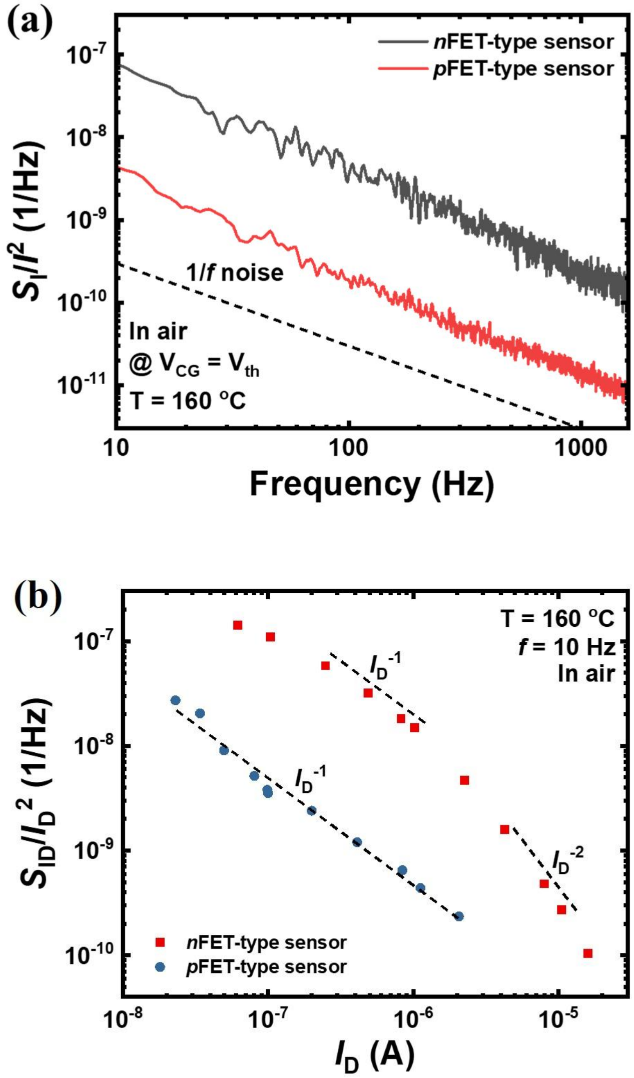

Fig. 3.21. (a) Normalized drain current noise power spectral densities (S_{ID}/I_D^2s) of the nFET-type and pFET-type sensors measured at $V_{CG} = V_{th}$ and 160 °C. (b) The log-log plot of S_{ID}/I_D^2s sampled at 10 Hz versus I.

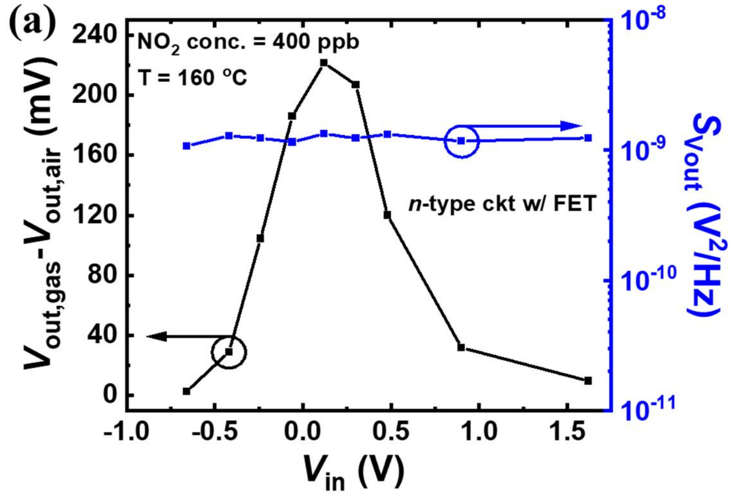

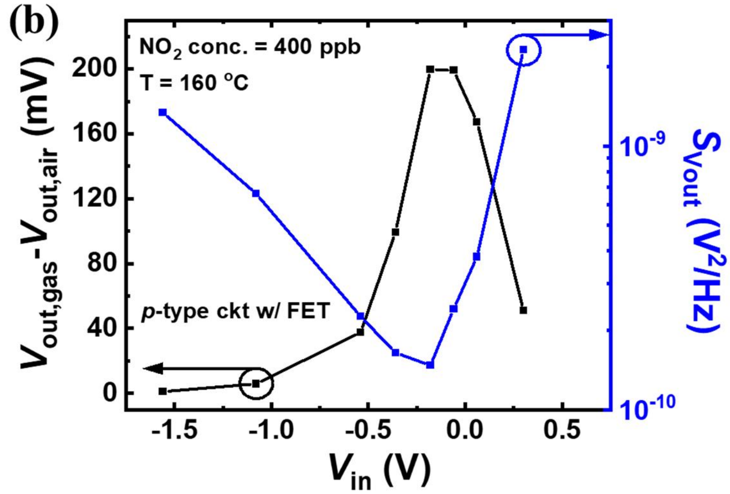

Fig. 3.22. $V_{\mathrm{out,gas}}$ - $V_{\mathrm{out,air}}$ and the output voltage noise (S_{Vout}) of the (a) *n*-type and (b) *p*-type amplifier circuits with FET loads as a function of V_{in} at 160 °C. The S_{Vout} of the *n*-type amplifier circuit shows no dependence on V_{in}. The S_{Vout} of the *p*-type amplifier circuit is minimum when V_{in} is 0 V.

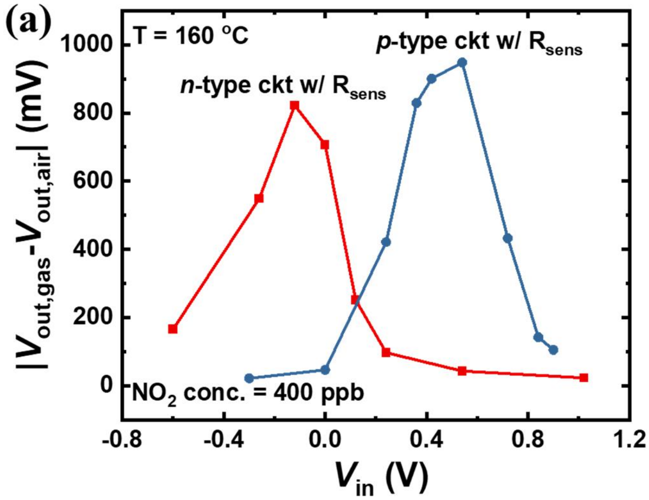

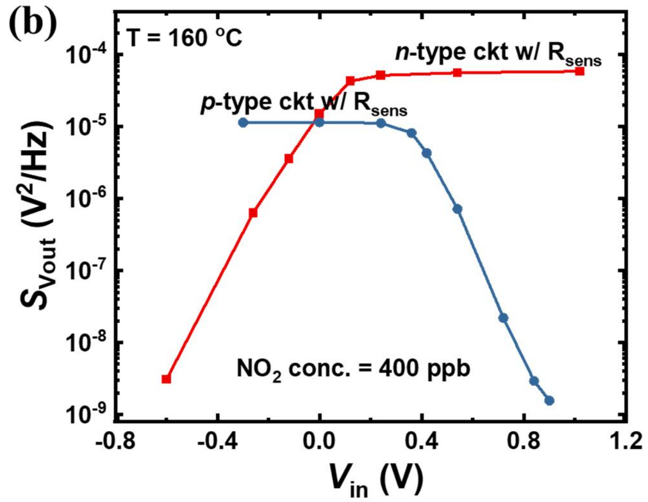

Fig. 3.23. (a) $|V_{out,gas} - V_{out,air}|$ and (b) the output voltage noise (S_{Vout}) of the *n*-type and *p*-type amplifier circuits with resistor-type sensors versus V_{in} at 160 ºC. The S_{Vout}s of the amplifier circuits are mainly determined by the noise of the resistor-type gas sensor.

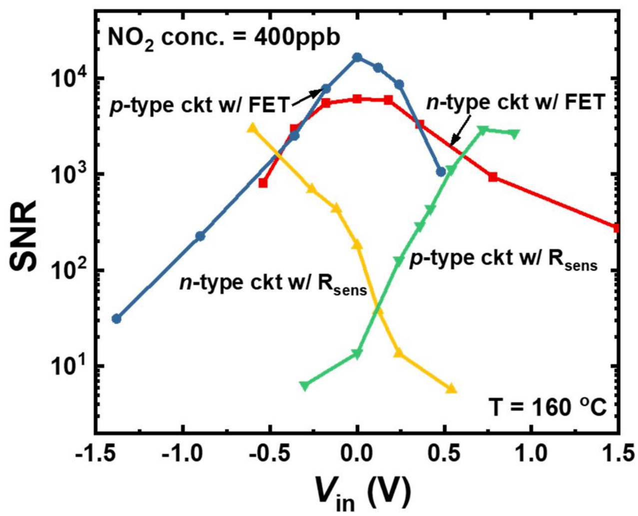

Fig. 3.24. SNR of four different amplifier circuits versus V_{in}. The noise and output signal of each circuit is measured at 160 ºC.

Chapter 4

Inverter circuit composed of gas sensors

4.1 Electrical and sensing characteristics of inverter circuit

A CMOS inverter circuit with gas sensors is fabricated, connecting the *n*FET- and *p*FET-type gas sensors in series. Fig. 4.1 shows the transfer (V_{out}-V_{in}) curves of the fabricated inverter circuit with *n*FET- and *p*FET-type sensors as a parameter of the V_{DD} (0.8 V ~ 2.0 V) at 20 ºC. In this inverter circuit, the W/Ls of the *n*FET- and *p*FET-type sensors are 2 μm/2 μm and 2 μm/1 μm, respectively. As shown in Fig. 4.1, the inverter circuit shows excellent inverting performance with the abrupt transition. The logic transition of the inverter circuit occurs at the switching threshold voltage where the V_{in} and V_{out} are equal. The voltage gain of the inverter circuit is approximately 35 at V_{DD} = 1.5 V.

Fig. 4.2 shows a schematic illustration deriving operating points of the CMOS inverter circuit before and after the NO_2 gas response using load-line analysis. The current flowing through the nFET- and pFET-type sensors in the inverter circuit should be the same. Therefore, V_{out} is determined at the point where the currents of the nFET- and pFET-type sensors are the same in the load-line analysis. In Fig. 4.2, the solid and dotted lines indicate the transfer curve ($|I_D|$-V_{DS}) of the FET-type sensors before and after gas response, respectively. As mentioned above, the current of the nFET-type sensor decreases, and that of the pFET-type sensor increases when the inverter circuit is exposed to NO_2 gas. Therefore, the V_{out} determined by the load-line analysis is shifted to the positive bias direction, as shown in Fig. 4.2. Fig. 4.3(a) shows the transfer curve (V_{out}-V_{in}) of the inverter circuit composed of the nFET- and pFET-type sensors as a parameter of NO_2 gas concentration (0 ppb ~ 500 ppb) at 120 ºC. As the inverter circuit responds to NO_2 gas, the transfer curve of the inverter circuit is shifted to the positive bias direction. Then, the output voltage of the circuit increases at the same input voltage. The output voltage of the inverter circuit changes as much as the sum of the current changes of both FET-type sensors since the currents of both FET-type sensors change due to gas response. Therefore, the amount of change in the output voltage due to gas response is larger than that of a circuit consisting of only one sensor. The ΔVout of the inverter circuit is 1.44 V at a V_{DD} of 1.5 V when exposed to 500 ppb of NO_2 gas.

On the other hand, the current of the *n*FET-type sensor increases, and that of the *p*FET-type sensor decreases when the inverter circuit is exposed to H_2S gas. Fig. 4.4 shows a schematic illustration deriving operating points of the CMOS inverter circuit before and after the H_2S gas response using load-line analysis. In Fig. 4.4, the solid and dotted lines indicate the transfer curve ($|I_D|$-V_{DS}) of the FET-type sensors before and after gas response, respectively. As shown in Fig. 4.4, the V_{out} determined by the load-line analysis is shifted to the negative bias direction when exposed to H_2S gas. Fig. 4.5(a) shows the transfer curve (V_{out}-V_{in}) of the inverter circuit composed of the *n*FET- and *p*FET-type sensors as a parameter of H_2S gas concentration (0 ppm ~ 50 ppm) at 160 °C. As the inverter circuit responds to NO_2 gas, the transfer curve of the inverter circuit is shifted to the negative bias direction. Then, the output voltage of the circuit decreases at the same input voltage. The ΔVout of the inverter circuit is 1.44 V at a V_{DD} of 1.5 V when exposed to 50 ppm of H_2S gas.

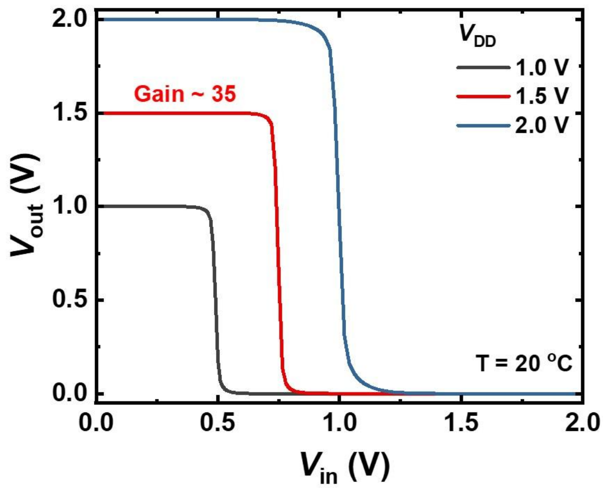

Fig. 4.1. Transfer (V_{out}-V_{in}) curves of the fabricated CMOS inverter with *n*FET- and *p*FET-type gas sensor as a parameter of the V_{DD} at room temperature.

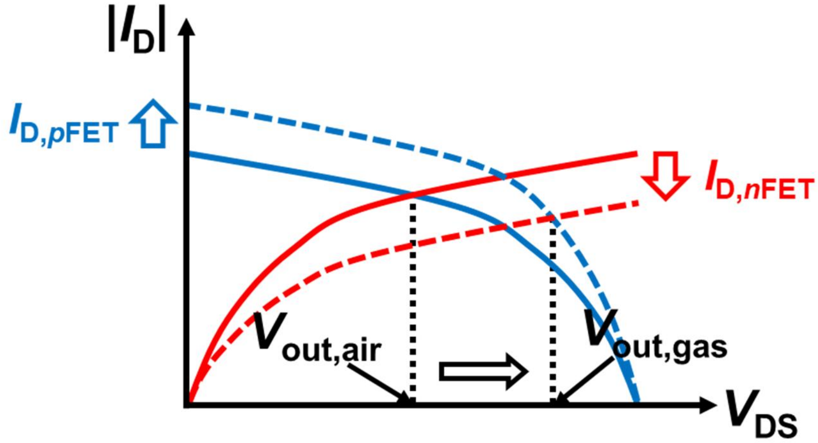

Fig. 4.2. Schematic illustration deriving operating points of the CMOS inverter circuit before and after NO_2 gas response using load-line analysis.

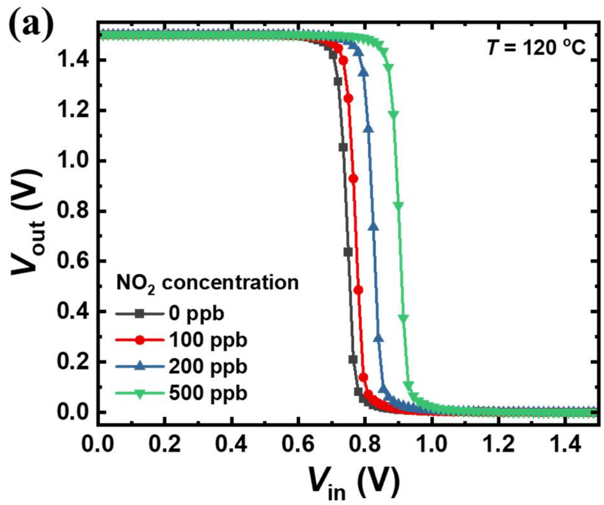

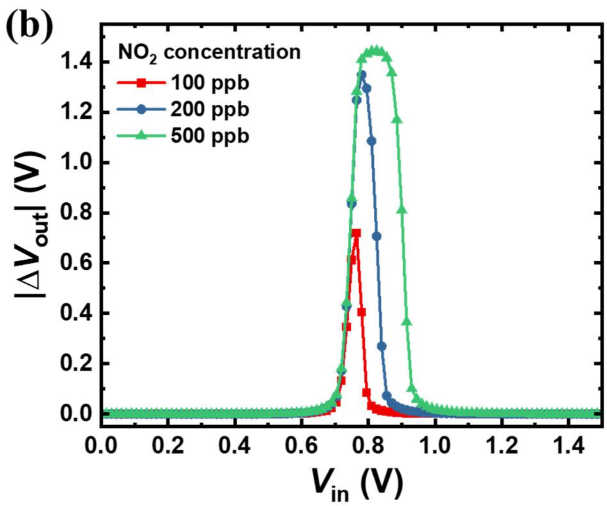

Fig. 4.3. (a) Transfer curves of the inverter circuit consisting of the *n*FET- and *p*FET-type gas sensors as a parameter of NO_2 concentration (0 ppb ~ 500 ppb) at 120 ºC. (b) ΔV_{out} (= $V_{out,gas}$ - $V_{out,air}$) of the inverter circuit versus V_{in} as a parameter of NO_2 concentration.

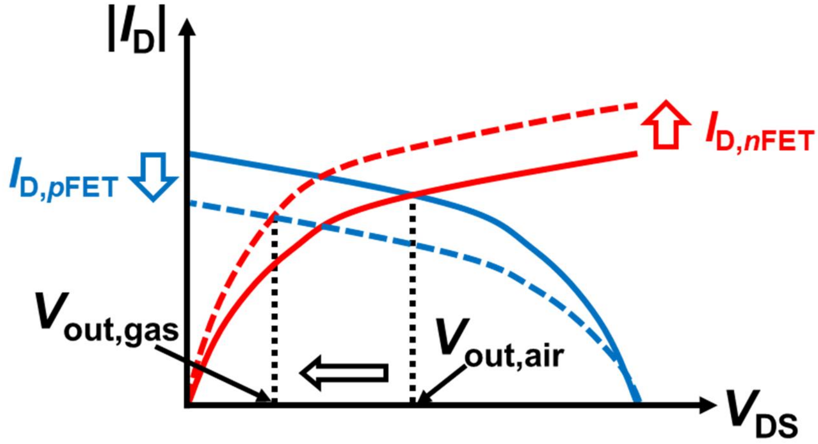

Fig. 4.4. Schematic illustration deriving operating points of the CMOS inverter circuit before and after H_2S gas response using load-line analysis.

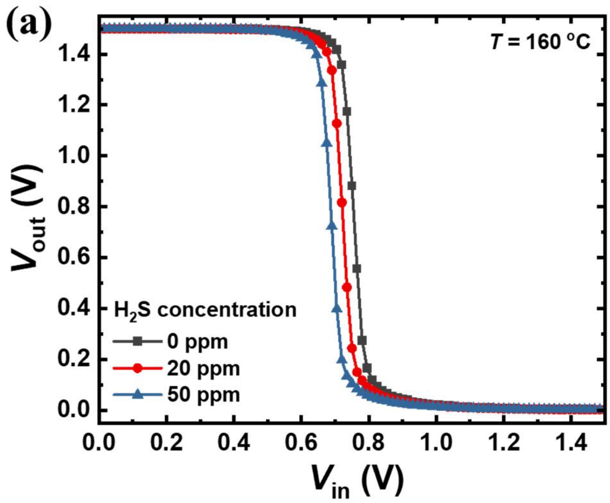

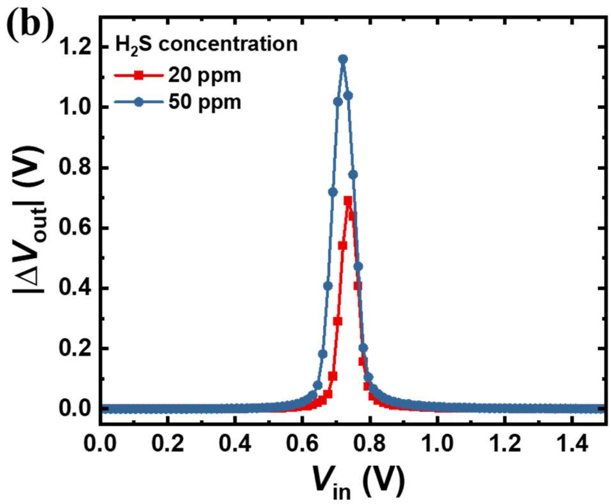

Fig. 4.5. (a) Transfer curves of the inverter circuit consisting of the *n*FET- and *p*FET-type gas sensors as a parameter of H_2S concentration (0 ppm ~ 50 ppm) at 160 ºC. (b) ΔV_{out} (= $V_{out,gas}$ - $V_{out,air}$) of the inverter circuit versus V_{in} as a parameter of H_2S concentration.

4.2 Application of inverter circuit

Fig. 4.6(a) shows the circuit schematic of the inverter circuit composed of the FET-type gas sensors for PWM operation. A triangular wave with a period of 200 ms is applied to the input of the inverter circuit. When a triangular wave is applied, the inverter circuit generates a logic pulse as an output voltage, as shown in Fig. 4.6(a). Fig. 4.6(b) shows the pulse schematic diagram of input and output voltage with different switching thresholds. As shown in Fig. 4.6(b), the width of the output voltage pulse is determined by the switching threshold voltage of the inverter circuit. As mentioned above, the switching threshold of the inverter circuit output voltage is changed by the sensor reaction when the inverter circuit is exposed to the gas molecules. The direction and degree of the switching threshold are adjusted according to the type and concentration of the gas molecules. Therefore, as shown in Fig. 4.6(b), the inverter circuit shows pulse width modulated behavior, in which the width of the output voltage pulse changes according to the type and concentration of the gas molecules.

Fig. 4.7(a) and (b) show V_{in} and V_{out} in the transient analysis of the CMOS inverter circuit when exposed to different concentrations of the NO_2 gas (0 ppb ~ 500 ppb). When exposed to the NO_2 gas, the transfer curve of the inverter circuit is shifted to the positive bias direction (Fig. 4.5(a)). As shown in Fig. 4.6(a), the switching threshold of the inverter circuit increases as the NO_2 gas concentration increases. Accordingly, the pulse width of the V_{out} decreases according to the NO_2 gas concentration. As shown in Fig. 4.6(b), the pulse width of the output voltage is adjusted by 36.29 ms as the NO_2 concentration changes from 0 ppb to 500 ppb.

Fig. 4.7(a) and (b) show V_{in} and V_{out} in the transient analysis of the CMOS inverter circuit when exposed to different concentrations of the H_2S gas (0 ppm ~ 50 ppm). When exposed to the H_2S gas, the transfer curve of the inverter circuit is shifted to the negative bias direction. As shown in Fig. 4.7(a), the switching threshold of the inverter circuit decreases as the H_2S gas concentration increases as opposed to the NO_2 gas reaction. Accordingly, the pulse width of the V_{out} increases according to the H_2S gas concentration. As shown in Fig. 4.7(b), the pulse width of the output voltage is adjusted by 13.42 ms as the H_2S concentration changes from 0 ppm to 50 ppm.

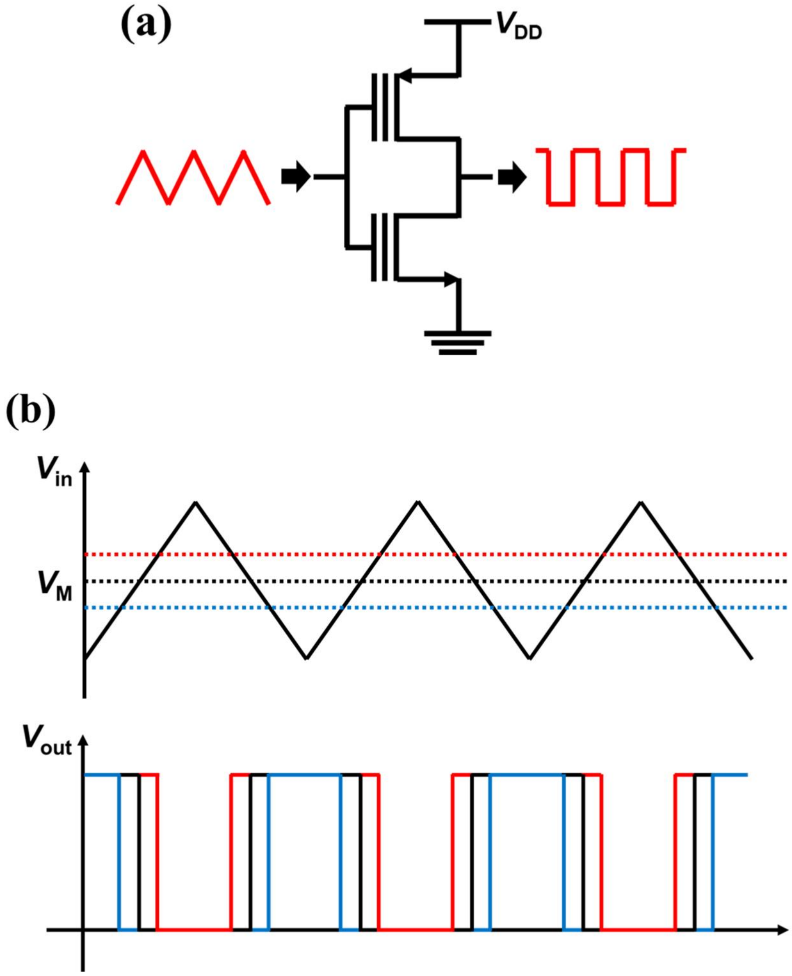

Fig. 4.6. (a) Circuit schematic of the inverter circuit composed of the FET-type gas sensors for PWM operation. (b) Pulse schematic diagram of input voltage (V_{in}) and V_{out} with different switching thresholds. When a triangular wave is applied to the input of the inverter circuit, the pulse width of the output voltage (V_{out}) is determined by the switching threshold.

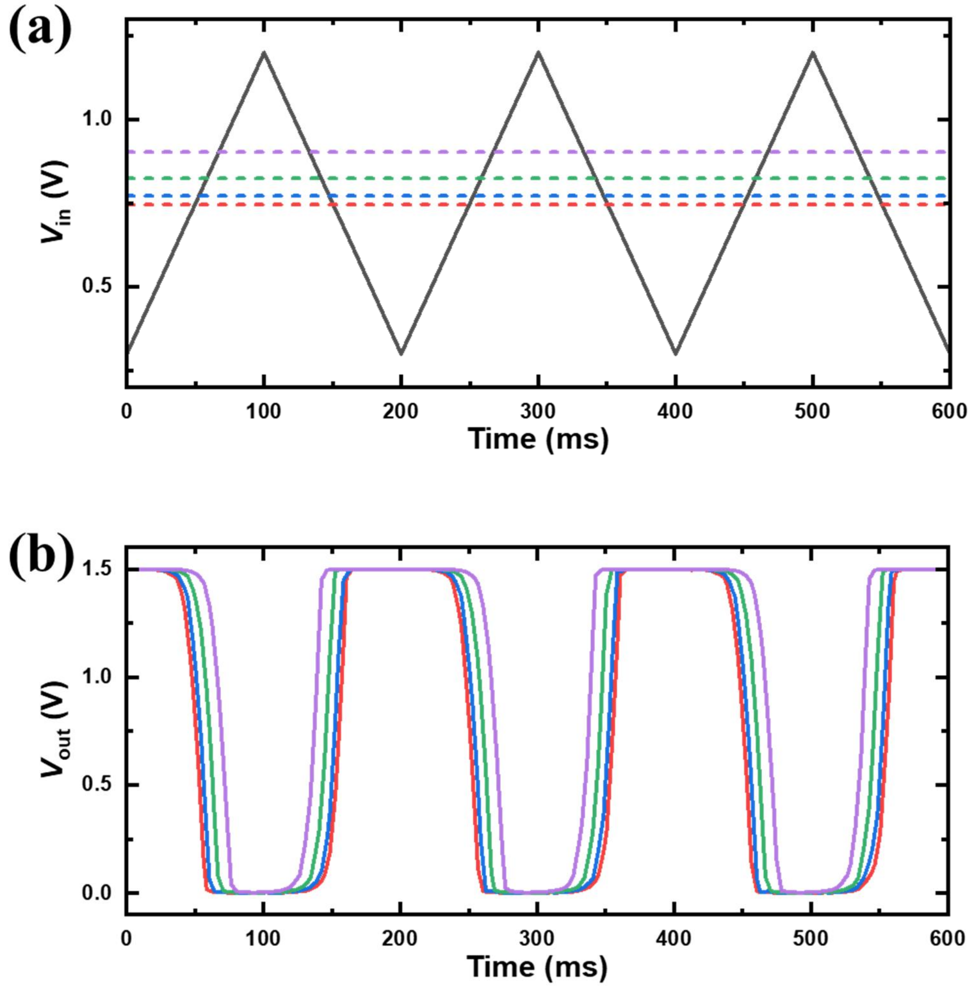

Fig. 4.7. (a) Input voltage (V_{in}) and (b) output voltage (V_{out}) in the transient analysis of the CMOS inverter circuit when exposed to different concentrations of the NO_2 gas (0 ppb ~ 500 ppb). In Fig. 4.7(a), dotted lines indicate the switching threshold of the circuit as a parameter of the NO_2 gas concentration.

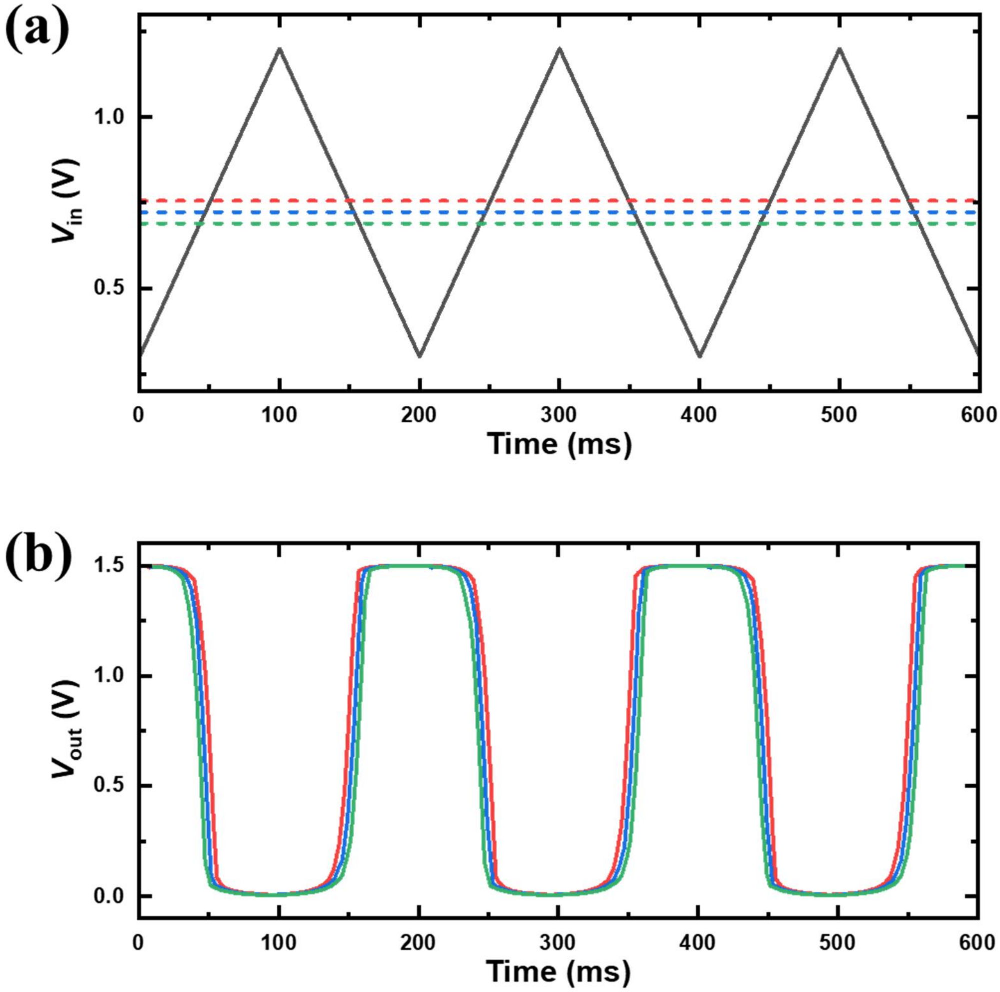

Fig. 4.8. (a) Input voltage (V_{in}) and (b) output voltage (V_{out}) in the transient analysis of the CMOS inverter circuit when exposed to different concentrations of the H_2S gas (0 ppm ~ 50 ppm). In Fig. 4.8(a), dotted lines indicate the switching threshold of the circuit as a parameter of the H_2S gas concentration.

Chapter 5

Conclusions

In this dissertation, the interface circuits using a gas sensor platform compatible with the conventional CMOS process are proposed. Especially in this dissertation, the interface circuits composed of complementary sensors are proposed. The *n*FET- and *p*FET-type gas sensors, FET elements, and resistor-type gas sensors are fabricated on the same substrate. The current of the complementary sensors is changed in the opposite direction in the same gas response. The electrical, gas sensing, and low-frequency noise characteristics of four different amplifier circuits are compared. When exposed to NO_2 gas, the current of *n*FET- and resistor-type gas sensors decreases, but the current of *p*FET-type gas sensor increases. The resistor-type sensor has more large sensitivity to the same concentration of NO_2 gas than the *n*FET- and *p*FET-type sensors.

When comparing the sensing characteristics of amplifier circuits, the amplifier circuits with the resistor-type sensor as a load has more large sensitivity. The *p*FET-type sensor has complementary sensing characteristics to the resistor-type sensor. Accordingly, the amplifier circuit with the *p*FET- and resistor-type sensors has the highest sensitivity. The output voltage of the amplifier circuit with the resistor-type sensor as a load is linear versus NO_2 gas concentration. Furthermore, the low-frequency noise characteristics of the amplifier circuit are analyzed. The S_{vout} of the amplifier circuit with the resistor-type sensor is determined by the noise behavior of the resistor-type sensor, making S_{Vout} of the circuit higher. Even so, the *p*-type amplifier circuit with a resistor-type sensor has a relatively excellent SNR, good linearity, and high sensitivity up to 8.96 mV/ppb.

The CMOS inverter circuit with *n*FET- and *p*FET-type sensors is manufactured, and the electrical and sensing characteristics are analyzed. The inverter circuit exhibits excellent inverting performances with a high voltage gain (> 35). Since the *p*FET-type sensor also has complementary sensing characteristics to the *n*FET-type sensor, the inverter circuit also has considerable sensitivity, like the *p*-type amplifier circuit with a resistor-type sensor. Also, the pulse width modulated behavior of the inverter circuit is confirmed. The pulse width of the output voltage in the inverter circuit is adjusted by the type and concentration of the gas molecules.

The sensitivity of an interface circuit composed of gas sensors having complementary sensing characteristics, such as the combination of a *p*FET- and resistor-type sensor and a *p*FET- and *n*FET-type sensor, is higher than that of other circuits. A *p*-type amplifier circuit with a resistor-type sensor shows linear sensitivity over a wide range of gas concentrations. On the other hand, the CMOS inverter circuit with a gas sensor has a more significant voltage gain than the amplifier circuit, so it has high sensitivity. However, the concentration range of the target gas that can be distinguished by the change in the output voltage of the circuit is limited since the transition region is narrow. Therefore, the *p*-type amplifier circuit with a resistor-type sensor can be used as an analog circuit that detects a wide range of gas concentrations. The CMOS inverter circuit can be used as a logic circuit, such as PWM operation according to gas reaction. Research on various interface circuits composed of gas sensors is expected to be the basis for future intelligent olfactory systems.

Appendix A

Various sensing materials

A.1 Tungsten disulfide (WO_3)

The transient response of the FET-type gas sensor to NO_2 gas between 200 ppb and 500 ppb at 180 ºC is shown in Fig. A.1. In sputtering procedure, the WO_3 sensing layer of the FET-type gas sensor is deposited at an oxygen flow rate of 3 sccm with 30 sccm argon gas. Since NO_2 gas is an oxidizing gas, the NO_2 gas molecules which adsorbed on the WO_3 sensing layer take electrons from the sensing layer [45]. As a result of the NO_2 gas molecules becoming ionized, ionized gas molecules act as an effective negative charge to generate a positive charge in the channel of the FET-type gas sensor [46]. Therefore, the FET-type gas sensor's threshold voltage (V_{th}) is moved in the positive direction, and the drain current of the sensor increases. As NO_2 concentration increases from 200 ppb to 500 ppb, sensitivity of the gas sensors with WO_3 sensing layer increases as shown in Fig. A.1.

A comparison of the FET-type gas sensor's sensing characteristics for three different target gases (NO_2, H_2S, and SO_2) is shown in Fig. A.2. The reponse of the gas sensor for H_2S and SO_2 gas are 4.84 % and 6.29%, respectively. Even though the concentration of NO_2 gas is only 500 ppb, the response of the gas sensor to NO_2 gas is more considerable than other gases (Fig. A.2). Thus, the FET-type gas sensor with WO_3 sensing layer has the highest selectivity for NO_2 gas.

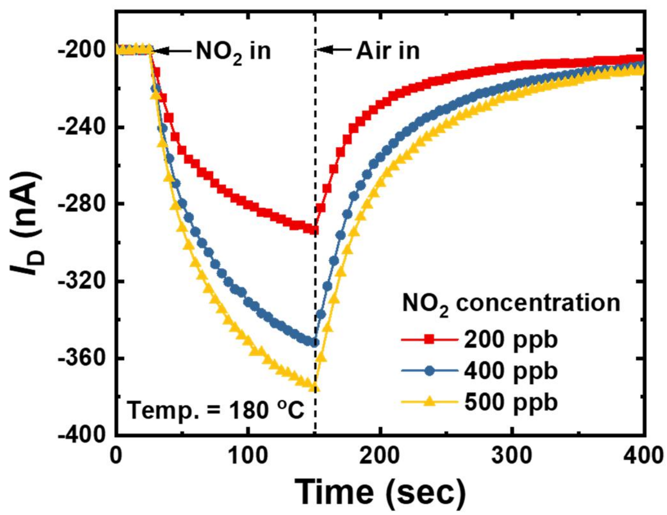

Fig. A.1. Transient sensing characteristics of the FET-type gas sensor with WO_3 sensing layer at 180 ºC. The WO_3 sensing layer of the gas sensor is deposited at an oxygen flow rate of 3 sccm with 30 sccm argon gas in the sputtering process.

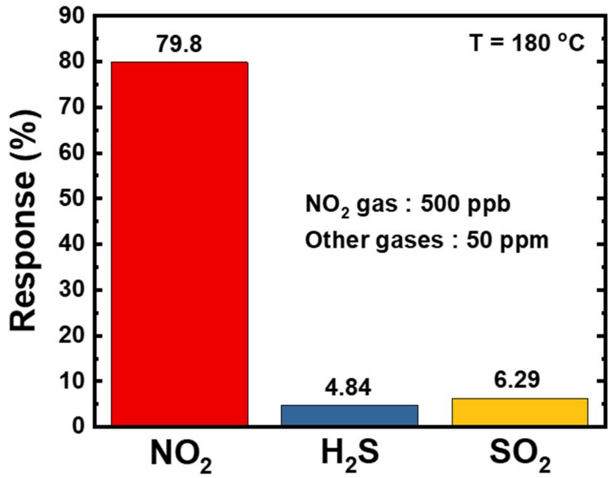

Fig. A.2. Comparison of the response of the FET-type gas sensor to the three different gases (NO_2, H_2S, and SO_2). The concentration of the NO_2 gas is 500ppb, and that of other gases is 50 ppm.

A.2 Graphene quantum dots (GQDs)

Fig. A.2 transfer curves (I_D–V_{CG}) of the FET-type humidity sensor with graphene quantum dots (GQDs) as a parameter of the relative humidity from 3.4% RH to 81.3% RH at 20 °C. The transfer curve is moved in the negative bias as the relative humidity increases from 3.4% to 81.3%. The H_2O molecules are chemisorbed on the GQDs sensing layer at low relative humidity [53,54]. The H_2O

molecules are poor oxidizing and reducing agents; therefore, how the H_2O molecules behave depends on the surroundings [55]. The H_2O molecules donate electrons to the GQDs sensing layer since the H_2O molecules act as an electron donor. As a result, the resistance of the GQDs sensing layer, a *p*-type material, increases [55-57]. The water molecules are adsorbed at the interface between ONO covering the FG and GQDs and then adsorbed water molecules are positively ionized. The positively ionized water molecules induce negative charges in the channel of the FET [58]. Thus, the threshold voltage (V_{th}) of the humidity sensor is moved in a negative bias direction. Then, the drain current of the *p*FET-type humidity sensor decreases as the relative humidity increases. The water molecules are physisorbed on the chemisorbed water molecules through hydrogen bonds as the relative humidity increases [53]. Multilayer water molecules are adsorbed when the relative humidity increases further and gradually shows liquid-like behaviors. The physisorbed water molecules in the liquid multilayer are ionized into the H_3O^+ ions as charge carriers under the electrostatic fields. Ionic conductivity generated by the Grotthus chain reaction enables proton hopping between adjacent water molecules [53]. The physisorbed water molecules can induce dipoles at the surface of the GQDs sensing layer. The work-function of the sensing layer is uniformly shifted upwards by a certain amount as a result of the induced dipoles [59,60]. Thus, as well as at low relative humidity, the V_{th} of the humidity sensor is shifted to the negative bias direction, and then I_D decreases at high relative humidity.

We analyze the reproducibility and long-term stability of the FET-type humidity sensor with the GQDs sensing layer. By repeatedly injecting the dry and humid air (81.3% RH) into the test chamber, the reproducibility of the humidity sensor is analyzed. Fig. A.4 shows the humidity sensing properties of the humidity sensor remain unchanged even after repeated short-term operation. The long-term stability of the humidity sensor is evaluated by injecting humid air with different relative humidity (28.3, 47.2, 62.1, and 81.3 %RH) once every month for five months (Fig. A.4). The humidity sensor has been exposed to the air for five months except when measuring the humidity sensing properties. As shown in Fig. A.4, even after more than five months, the response of the humidity sensor is almost constant in all ranges of relative humidity.

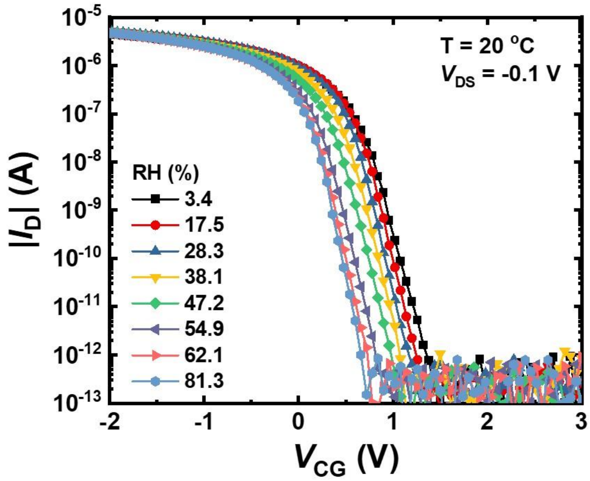

Fig. A.3. Transfer curves (I_D-V_{CG}) of the FET-type humidity sensor as a parameter of the relative humidity (from 17.5% RH to 81.3% RH) at 20 ºC.

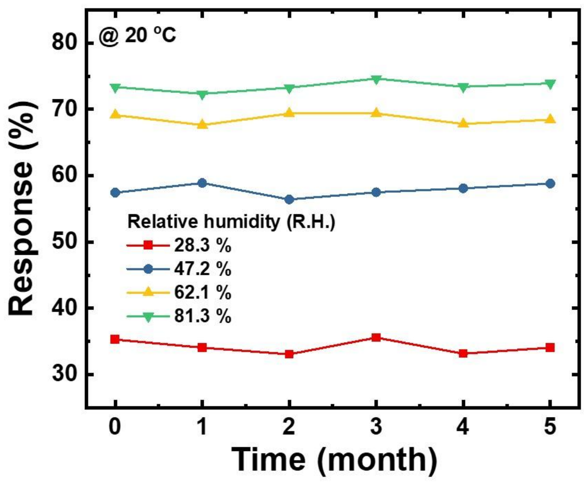

Fig. A.4. Long-term stability of the humidity sensor to the humid air. The response of the humidity sensor has no noticeable variation in all ranges of relative humidity levels even after more than five months.

Bibliography

[1] W. Tsujita, A. Yoshino, H. Ishida, and T. Moriizumi, "Gas sensor network for air-pollution monitoring," Sensors and Actuators B: Chemical, vol. 110, no. 2, pp. 304-311, Oct. 2005.

[2] S. Adaduzzaman and K. Ahmed, “Proposal of a gas sensor with high sensitivity, birefringence and nonlinearity for air pollution monitoring,” Sensing and Bio-Sensing Research, vol. 10, pp. 20-26, Sep. 2016.

[3] S. Olyaee, A. Naraghi, and V. Ahmadi, “High sensitivity evanescent-field gas sensor based on modified photonic crystal fiber for gas condensate and air pollution monitoring,” Optik, vol. 125, no. 1, pp. 596-600, Jan. 2014.

[4] Y. Suzuki, N. Nakano, and K. Suzuki, “Portable sick house syndrome gas monitoring system based on novel colorimetric reagents for the highly selective and sensitive detection of formaldehyde,” Environmental science & technology, vol. 37, no. 24, pp. 5695-5700, Nov. 2003

[5] K. Kawamura, K. Kerman, M. Fujihara, N. Nagatani, T. Hashiba, and E. Tamiya, “Development of a novel hand-held formaldehyde gas sensor for the rapid detection of sick building syndrome,” Sensors and Actuators B: Chemical, vol. 105, no. 2, pp. 495-501, Mar. 2005.

[6] C. Li, G. W. Krewer, P. Ji, H. Scherm, and S. J. Kays, “Gas sensor array for blueberry fruit disease detection and classification,” Postharvest Biology and Technology, vol. 55, no. 3, pp. 144-149, Mar. 2010.

[7] C. Di Natale, R. Paolesse, E. Martinelli, and R. Capuano, “Solid-state gas sensors for breath analysis: A review,” Analytica chimica acta, vol. 824, pp. 1-17, May. 2014.

[8] S. Sekimoto, H. Nakagawa, S. Okazaki, K. Fukuda, S. Asakura, T. Shigemori,

and S. Takahashi, “A fiber-optic evanescent-wave hydrogen gas sensor using palladium-supported tungsten oxide,” Sensors and Actuators B: Chemical, vol. 66, no. 1-3, pp. 142-145, Jul. 2000.

[9] H. Tai, H. Tanaka, and T. Yoshino, “Fiber-optic evanescent-wave methane-gas sensor using optical absorption for the 3.392-□m line of a He-Ne laser,” Optics Letters, vol. 12, no. 6, pp. 437-439, Jun. 1987.

[10] S. K. Mishra, S. N. Tripathi, V. Choudhary, and B. D. Gupta, “SPR based fibre optic ammonia gas sensor utilizing nanocomposite film of PMMA/reduced graphene oxide prepared by in situ polymerization,” Sensors and Actuators B: Chemical, vol. 199, pp. 190-200, Aug. 2014.

[11] N. Dossi, R. Toniolo, A. Pizzariello, E. Carrilho, E. Piccin, S. Battiston, and G. Bonetempelli, “An electrochemical gas sensor based on paper supported room temperature ionic liquids,” Lab on a Chip, vol. 12, no. 1, pp. 153-158, Jan. 2012.

[12] H. Li, X. Mu, Y. Yang, and A. J. Mason, “Low Power Multimode Electrochemical Gas Sensor Array System for Wearable Health and Safety Monitoring,” IEEE Sensors Journal, vol. 14, no. 10, pp. 3391-3399, Oct. 2014.

[13] M. J. Tierney and H. -O. L. Kim, “Electrochemical Gas Sensor with Extremely Fast Response Times,” Analytical Chemistry, vol. 65, no. 23, pp. 3435-3440, Sep. 1993.

[14] S. Pandey, G. K. Goswami, and K. K. Nanda, “Nanocomposite based flexible ultrasensitive resistive gas sensor for chemical reactions studies,” Scientific Reports, vol. 3, no. 1, pp. 1-6, Jun. 2013.

[15] R. Moos, F. Rettig, A. Hürland, and C. Plog, “Temperature-independent resistive oxygen exhaust gas sensor for lean-burn engines in thick-film technology,” Sensors and Actuators B: Chemical, vol. 93, no. 1-3, pp. 43-50, Aug. 2003.

[16] Y. Jeong, J. Shin, Y. Hong, M. Wu, S. Hong, K. C. Kwon, S. Choi, T. Lee, H.

W. Jang, and J. H. Lee, “Gas sensing characteristics of the FET-type gas sensor having inkjet-printed WS_2 sensing layer,” Solid-State Electronics, vol. 153, pp. 27-32, Mar. 2019.

[17] R. Yoshimura, M. Kohtoku, K. Fujii, T. Sakamoto, and Y. Sakai, “ Highly Sensitive Laser Based Trace-gas Sensor Technology and Its Application to Stable Isotope Ratio Analysis,” NTT Technical Review, vol. 12, no. 4, pp. 1-6, Apr. 2014.

[18] R. Rubio, J. Santander, L. Fonseca, N. Sabaté, I. Gràcia, C. Cané, S. Udina, and S. Marco, “Non-selective NDIR array for gas detection,” Sensors and Actuators B: Chemical, vol. 127, no. 1, pp. 69-73, Oct. 2007.

[19] O. A. M. Popoola, G. B. Stewart, M. I. Mead, and R. L. Jones, “Development of a baseline-temperature correction methodology for electrochemical sensors and its implications for long-term stability,” Atmospheric Environment, vol. 147, pp. 330-343, Dec. 2016.

[20] T. Hübert, L. Boon-Brett, G. Black, and U. Banach, “Hydrogen sensors – A review,” Sensors and Actuators B: Chemical, vol. 157, pp. 329-352, Oct. 2011.

[21] P. Rai, S. M. Majhi, Y. -T. Yu, and J. -H. Lee, “Noble metal@metal oxide semiconductor core@shell nano-architectures as a new platform for gas sensor applications,” RSC advances, vol. 5, no. 93, pp. 76229-76248, Aug. 2015.

[22] S. Mishra, C. Ghanshyam, N. Ram, R. P. Bajpai, and R. K. Bedi, “Detection mechanism of metal oxide gas sensor under UV radiation,” Sensors and Actuators B: Chemical, vol. 97, no. 2-3, pp. 387-390, Feb. 2004.

[23] K. T. Ng, F. Bousssaid, and A. Bermak, “A CMOS Single-Chip Gas Recognition Circuit for Metal Oxide Gas Sensor Arrays,” IEEE Transactions on Circuits and Systems I: Regular Papers, vol. 58, no. 7, pp. 1569-1580, Jul. 2011.

[24] S. Peng, K. Cho, P. Qi, and H. Dai, “Ab initio study of CNT NO2 gas sensor,” Chemical Physics Letters, vol. 387, no. 4-6, pp. 271-276, Apr. 2004.

[25] D. Kumar, P. Chaturvedi, P. Saho, P. Jha, A. Chouksey, M. Lal, J. S. B. S. Rawat, R. P. Tandon, and P. K. Chaudhury, “Effect of single wall carbon nanotube networks on gas sensor response and detection limit,” Sensors and Actuators B: Chemical, vol. 240, pp. 1134-1140, Mar. 2017.

[26] R. K. Paul, S. Badhulika, N. M. Saucedo, and A. Mulchandani, “Graphene Nanomesh As Highly Sensitive Chemiresistor Gas Sensor,” Analytical Chemistry, vol. 84, no. 19, pp. 8171-8178, Oct. 2012.

[27] D. J. Late, T. Doneux, and M. Bougouma, “Single-layer MoSe2 based NH3 gas sensor,” Applied Physics Letters, vol. 105, no. 23, p. 233103, Dec. 2014.

[28] K. Y. Ko, S. Lee, K. Park, Y. Kim, W. J. Woo, D. Kim, J. -G. Song, J. Park, J. H. Kim, Z. Lee, and H. Kim, “High-Performance Gas Sensor Using a Large-Area WS2xSe2–2x Alloy for Low-Power Operation Wearable Applications,” ACS Applied Materials & Interfaces, vol. 10, no. 40, pp. 34163-34171, Oct. 2018.

[29] A. V. Agrawal, N. Kumar, and M. Kumar, “Strategy and Future Prospects to Develop Room-Temperature-Recoverable NO2 Gas Sensor Based on Two-Dimensional Molybdenum Disulfide,” Nano-Micro Letters, vol. 13, no. 1, pp. 1-58, Jan. 2021.

[30] H. Long, A. Harley-Trochimczyk, T. He, T. Pham, Z. Tang, T. Shi, A. Zettl, W. Mickelson, C. Carraro, and R. Maboudian, “In situ localized growth of porous tin oxide films on low power microheater platform for low temperature CO detection,” ACS Sensors, vol. 1, no. 4, pp. 339–343, Apr. 2016.

[31] C. -H. Kim, I. -T. Cho, J. -M. Shin, K. -B. Choi, J. -K. Lee, and J. -H. Lee, “A New Gas Sensor Based on MOSFET Having a Horizontal Floating-Gate,” IEEE Electron Device Letters, vol. 35, no. 2, pp. 265-267, Feb. 2014.

[32] S. Hong, M. Wu, Y. Hong, Y. Jeong, G. Jung, W. Shin, J. Park, D. Kim, D. Jang, and J. -H. Lee, “FET-type gas sensors: A review,” Sensors and Actuators B:

Chemical, vol. 330, p. 129240, Mar. 2021.

[33] Y. Hong, S. Hong, D. Jang, Y. Jeong, M. Wu, G. Jung, J. -H. Bae, J. S. Kim, K. S. Chang, C. B. Jeong, C. S. Hwang, B. -G. Park, and J. -H. Lee, "A Si FET-type Gas Sensor with Pulse-driven Localized Micro-heater for Low Power Consumption," Proceedings of 2018 IEEE International Electron Devices Meeting (IEDM), San Francisco, CA, USA, Dec. 2018.

[34] Y. Jeong, W. Shin, S. Hong, G. Jung, J. Park, D. Jang, D. Kim, D. Kwon, B. -G. Park, and J. -H. Lee, "Highly Sensitive Amplifier Circuit Consisting of Complementary pFET-type and Resistor-type Gas Sensors," Proceedings of 2020 IEEE International Electron Devices Meeting (IEDM), San Francisco, CA, USA, Dec. 2020.

[35] C. Hagleitner, A. Hierlemann, D. Lange, A. Kummer, N. Kerness, O. Brand, and H. Baltes, "Smart single-chip gas sensor microsystem," Nature, vol. 414, no. 6861, pp. 293-296, Nov. 2001.

[36] J. W. Gardner, P. K. Guha, F. Udrea, J. A. Covington, "CMOS interfacing for integrated gas sensors: A review," IEEE Sensors Journal, vol. 10, no. 12, pp.1833-1848, Dec. 2010.

[37] J. Lee, J. M. Lee, J. H. Lee, W. H. Lee, M. Uhm, B. -G. Park, D. M. Kim, Y. -J. Jeong, and D. H. Kim, "Complementary silicon nanowire hydrogen ion sensor with high sensitivity and voltage output," IEEE electron device letters, vol. 33, no. 12, pp. 1768-1770, Dec. 2012.

[38] H. V. Shurmer, P. Corcoran, and M. K. James, "Sensitivity enhancement for gas sensing and electronic nose applications," Sensors and Actuators B: Chemical, vol. 16, no. 1-3, pp. 256-259, Oct. 1993.

[39] M. Cole, J. W. Gardner, A. W. Y. Lim, P. K. Scivier, and J. E. Brignell, "Polymeric resistive bridge gas sensor array driven by a standard cell CMOS

current drive chip," Sensors and Actuators B: Chemical, vol. 58, no. 1-3, pp. 518-525, Sep. 1999.

[40] K. Arshak, G. Lyons, L. Cavanagh, and S. Clifford, "Front-end signal conditioning used for resistance-based sensors in electronic nose systems: a review," Sensor Review, vol. 23, no.3, Sep. 2003.

[41] Q. Cheng, M. Wang, M. Tao, R. Yin, Y. Li, N. Yang, W. Xu, C. Gao, Y. Hao, and Z. Yang, "Planar dual gate GaN HEMT cascode amplifier as a voltage readout pH sensor with high and tunable sensitivities," IEEE Electron Device Letters, vol. 41, no. 3, pp. 485-488, Jan. 2020.

[42] M. T. Vijjapu, S. G. Surya, S. Yuvaraja, X. Zhang, H. N. Alshareef, and K. N. Salama, "Fully integrated indium gallium zinc oxide NO_2 gas detector," Acs Sensors, vol. 5, no. 4, pp. 984-993, Feb. 2020.

[43] H. Fan, H. Li, J. Han, N. McKeever, J. Yu, and H. E. Katz, "A humid-air-operable, NO_2-responsive polymer transistor series circuit with improved signal-to-drift ratio based on polymer semiconductor oxidation," ACS sensors, vol. 4, no. 12, pp. 3240-3247, Nov. 2019.

[44] P. C. Jong, G. C. M. Meijer, and A. H. M. Roermund, "A 300℃ Dynamic-Feedback Instrumentation Amplifier", IEEE J. Solid State Circuits, Vol. 33, pp. 1999-2009, 1998.

[45] D. Han, L. Zhai, F. Gu, and Z. Wang, "Highly sensitive NO_2 gas sensor of ppb-level detection based on In_2O_3 nanobricks at low temperature," Sensors and Actuators B: Chemical, vol. 262, pp. 655-663, Jun. 2018.

[46] W. Shin, G. Jung, S. Hong, Y. Jeong, J. Park, D. Kim, D. Jang, D. Kwon, J. -H. Bae, B. -G. Park, and J. -H. Lee, "Proposition of deposition and bias conditions for optimal signal-to-noise-ratio in resistor-and FET-type gas sensors," Nanoscale, vol. 12, no. 38, pp. 19768-19775, Sep. 2020.

[47] S. Gomri, J. L. Seguin, J. Guerin, and K. Aguir, "Adsorption–desorption noise in gas sensors: Modelling using Langmuir and Wolkenstein models for adsorption," Sensors and Actuators B: Chemical, vol. 114, no. 1, pp. 451-459, Mar. 2006.

[48] M. Kaur, N. Jain, K. Sharma, S. Bhattacharya, M. Roy, A. K. Tyagi, S. K. Gupta, and J. V. Yakhmi, "Room-temperature H2S gas sensing at ppb level by single crystal In2O3 whiskers," Sensors and Actuators B: Chemical, vol. 133, no. 2, pp. 456-461, Aug. 2008.

[49] G. Ghibaudo, "On the theory of carrier number fluctuations in MOS devices," Solid-State Electronics, vol. 32, pp. 563-565, Jul. 1989.

[50] G. Ghibaudo, O. Roux, C. Nguyen-Duc, F. Balestra, and J. Brini, "Improved analysis of low frequency noise in field-effect MOS transistors," Physica Status Solidi (a), vol. 124, no. 2, pp. 571-581, Apr. 1991.

[51] F. N. Hooge, "1/f noise sources," IEEE Transactions on electron devices, vol. 41, no. 11, pp. 1926-1935, Nov. 1994.

[52] E. G. Ioannidis, S. Haendler, C. A. Dimitriadis, and G. Ghibaudo, "Characterization and modeling of low frequency noise in CMOS inverters," Solid State Electronics, vol. 81, pp. 151-156, Mar. 2013.

[53] A. Vergara, S. Vembu, T. Ayhan, M. A. Ryan, M. L. Homer, and R. Huerta, "Chemical gas sensor drift compensation using classifier ensembles," Sensors and Actuators B: Chemical, vol. 166, pp. 320-329, May. 2012.

[54] T. Alizadeh and M. Shokri, "A new humidity sensor based upon graphene quantum dots prepared via carbonization of citric acid," Sensors and Actuators B: Chemical, vol. 222, pp. 728-734, Jan. 2016.

[55] S. Papamatthaiou, D. P. Argyropoulos, F. Farmakis, and N. Georgoulas, "Investigation of the H_2O Sensing Mechanism of DC-Operated Chemiresistors Based on Graphene Oxide and Thermally Reduced Graphene Oxide," IEEE Sensors

Journal, vol. 19, no. 18, pp. 7841-7848, Jun. 2019.

[56] C. O. Kim, S. W. Hwang, S. Kim, D. H. Shin, S. S. Kang, J. M. Kim, C. W. Jang, J. H. Kim, K. W. Lee, S. H. Choi, and E. Hwang, “High-performance graphene-quantum-dot photodetectors,” Scientific Reports, vol. 4, pp. 5603, Jul. 2014.

[57] S. Y. Park, Y. H. Kim, S. Y. Lee, W. Sohn, J. E. Lee, Y. S. Shim, K. C. Kwon, K. S. Choi, H. J. Yoo, J. M. Suh, M. Ko, J. H. Lee, M. J. Lee, S. Y. Kim, M. H. Lee, and H. W. Jang, “Highly selective and sensitive chemoresistive humidity sensors based on rGO/MoS_2 van der Waals composites,” Journal of Materials Chemistry A, vol. 6, pp. 5016-5024, Mar. 2018.

[58] S. Hong, Y. Hong, Y. Jeong, G. Jung, W. Shin, J. Park, J. K. Lee, D. Jang, J.-H. Bae, and J.-H. Lee, “Improved CO gas detection of Si MOSFET gas sensor with catalytic Pt decoration and pre-bias effect,” Sensors and Actuators B: Chemical, vol. 300, pp. 127040, Dec. 2019.

[59] M. Wu, Z. Wu, X. Jin, and J.-H. Lee, “A Highly Sensitive FET-Type Humidity Sensor with Inkjet-Printed Pt-In_2O_3 Nanoparticles at Room Temperature,” Nanoscale Research Letters, vol. 15, pp. 1-8, Oct. 2020.

[60] S. Hong, J. Shin, Y. Hong, M. Wu, D. Jang, Y. Jeong, G. Jung, J.-H. Bae, H. W. Jang, and J.-H. Lee, “Observation of physisorption in a high-performance FET-type oxygen gas sensor operating at room temperature,” Nanoscale, vol. 10, pp. 18019-18027, Sep. 2018.

초 록

최근 급속한 산업화의 발전에 따라 운송 수단 및 건축 자재 등으로부터 나오는 유해 가스로 인해 실내외 대기 오염이 심화되고 있다. 이에 따라, 실내외 대기질을 모니터링할 수 있는 가스 센서에 대한 필요성이 대두되고 있다. 이러한 수요에 발맞춰, 많은 연구 그룹에서는 광학식, 전기화학식, 반도체식 가스 센서 등 다양한 가스 센서 플랫폼에 대한 연구를 하고 있다. 그 중에서도 저항형 가스 센서는 비교적 큰 감도, 간단한 공정 과정, 값싼 비용의 장점을 가지고 있어 많이 연구되고 있다. 그러나 저항형 가스 센서는 충분한 동작 전류 및 감도를 갖기 위해서 크기가 커져야 하고, 이에 따라 전력 소모도 증가한다는 단점을 갖는다. 이를 해결하기 위해 우리 연구 그룹에서는 수평형 플로팅 게이트를 갖는 전계 효과 트랜지스터 (FET) 가스 센서를 제안하였다. 이 FET 가스 센서는 저전력으로 동작하고 상보형 금속 산화막 반도체 (CMOS) 공정과 호환이 가능하기 때문에 CMOS 기반의 인터페이스 회로 및 프로세서와 집적이 가능하다는 장점을 갖는다.

본 논문에서는 기존의 CMOS 공정과 호환이 가능한 가스 센서 플랫폼을 사용한 인터페이스 회로를 제안한다. 가스 센서 플랫폼은 n형 및 p형 채널을 갖는 FET 가스 센서와 FET 소자 그리고 저항형 가스 센서를 포함하고 있으며, 이는 모두 동일한 기판에 제작된다. 특히 본 논문에서는 서로 상보적인 감지 특성을 갖는 가스 센서를 사용한 인터페이스 회로를 제안한다. 서로 상보적인 감지 특성을 갖는 가스 센서는

동일한 가스에 반응하였을 때 전류가 서로 반대 방향으로 변화한다. 이 상보적인 감지 특성을 갖는 가스 센서로 구성된 증폭기 회로의 우수성을 입증하기 위해 다양한 증폭기 회로와 감도 및 신호 대 잡음비 (SNR) 측면에서 비교하였다. 또한, *p*FET 및 *n*FET 센서를 사용한 인버터 회로의 전기적 특성 및 감도를 조사하였다. 이 회로를 활용하여 가스의 종류와 농도에 따라 출력 전압 펄스의 폭이 조절되는 동작을 확인하였다.

*p*FET형과 저항형 센서, 그리고 *p*FET형과 *n*FET형 센서의 조합과 같이 서로 상보적인 감지 특성을 갖는 가스 센서들로 구성된 인터페이스 회로의 감도는 다른 회로 대비 훨씬 큰 값을 갖는다. *p*FET형과 저항형 센서로 구성된 증폭기 회로는 넓은 범위의 가스 농도에 대해 선형적인 특성을 보였다. 반면에 *p*FET형과 *n*FET형 센서로 구성된 CMOS 인버터 회로는 증폭기 회로에 비해 큰 전압 이득을 갖고 있으므로, 가스 반응에 대해 큰 감도를 갖는다. 그러나 CMOS 인버터 회로는 transfer 커브의 전이 구간이 좁기 때문에 출력 전압의 변화량으로 구별할 수 있는 가스의 농도가 제한적이다. 따라서, *p*FET형과 저항형 센서로 구성된 증폭기 회로는 넓은 범위의 가스를 감지할 수 있는 아날로그 회로로 활용할 수 있으며, CMOS 인버터 회로는 가스 반응에 따라 펄스의 폭이 조절되는 동작과 같이 로직 회로로 활용할 수 있다. 이렇게 가스 센서로 구성된 다양한 인터페이스 회로에 대한 연구는 미래 지능형 후각 시스템의 기반이 될 것으로 기대된다.

주요어 : FET형 가스 센서, 증폭기 회로, CMOS, 인버터 회로, 상보적인, 저주파 노이즈

학번 : 2017-24278

List of Publications

Journals

1. *Gyuweon Jung, *Seongbin Hong, Wonjun Shin, **Yujeong Jeong**, Jinwoo Park, Donghee Kim, and Jong-Ho Lee, "Design Optimization of FET-type Gas Sensor Considering Device Characteristics, Sensitivity, Power, Noise, and SNR," *Sensors and Actuators B: Chemical*, vol. 369, p. 132257, Oct. 2022.
2. *Wonjun Shin, ***Yujeong Jeong**, Seongbin Hong, Gyuweon Jung, Jinwoo Park, Donghee Kim, Byung-Gook Park, and Jong-Ho Lee, "Fully Integrated FET-type Gas Sensor with Optimized Signal-to-Noise Ratio for H_2S Gas Detection," *Sensors and Actuators B: Chemical*, vol. 367, p. 132052, Sep. 2022.
3. *Wonjun Shin, *Jiyoung Yim, Jong-Ho Bae, Jung-Kyu Lee, Seongbin Hong, Jaehyeon Kim, **Yujeong Jeong**, Dongseok Kwon, Ryun-Han Koo, Gyuweon Jung, Changhyeon Han, Jeonghan Kim, Byung-Gook Park, Daewoong Kwon, and Jong-Ho Lee, "Synergistic Improvement of Sensing Performance in Ferroelectric Transistor Gas Sensors Using Remnant Polarization," *Materials Horizons*, vol. 9, no. 6, pp. 1623-1630, Jun. 2022.
4. Jinwoo Park, Gyuweon Jung, Seongbin Hong, **Yujeong Jeong**, Wonjun Shin, Donghee Kim, Chayoung Lee, and Jong-Ho Lee, "Analysis of Cr/Au Contact Reliability in Embedded Poly-Si Micro-heater for FET-type Gas Sensor," *Sensors and Actuators B: Chemical*, vol. 360, p. 131673, Jun. 2022.
5. Wonjun Shin, Seongbin Hong, **Yujeong Jeong**, Gyuweon Jung, Byung-Gook Park, and Jong-Ho Lee, "Effects of Postdeposition Annealing Ambience on NO_2 Gas Sensing Performance in Si-Based FET-Type Gas Sensor," *IEEE Transactions on Electron Devices*, vol. 69, no. 5, pp. 2604-

2610, May 2022.

6. Gyuweon Jung, Seongbin Hong, **Yujeong Jeong**, Wonjun Shin, Jinwoo Park, Donghee Kim, and Jong-Ho Lee, "Highly Selective and Low-Power Carbon Monoxide Gas Sensor Based on the Chain Reaction of Oxygen and Carbon Monoxide to WO_3," *ACS Applied Materials & Interfaces*, vol. 14, no. 15, pp. 17950-17958, Apr. 2022.

7. Donghee Kim, Wonjun Shin, Seongbin Hong, **Yujeong Jeong**, Gyuweon Jung, Jinwoo Park, and Jong-Ho Lee, "Effects of Electrode Structure on H_2S Sensing and Low-frequency Noise Characteristics in In_2O_3-based Resistor-type Gas Sensors," *IEEE Sensors Journal*, vol. 22, no. 7, pp. 6311-6320, Apr. 2022.

8. *Wonjun Shin, *Gyuweon Jung, Seongbin Hong, **Yujeong Jeong**, Jinwoo Park, Donghee Kim, Byung-Gook Park, and Jong-Ho Lee, "Optimization of Channel Structure and Bias Condition for Signal-to-Noise Ratio Improvement in Si-based FET-type Gas sensor with Horizontal Floating-Gate," *Sensors and Actuators B: Chemical*, vol. 357, p. 131398, Apr. 2022.

9. Wonjun Shin, Seongbin Hong, **Yujeong Jeong**, Gyuweon Jung, Jinwoo Park, Donghee Kim, Byung-Gook Park, and Jong-Ho Lee, "Effects of Channel Length Scaling on the Signal-to-Noise Ratio in FET-Type Gas Sensor with Horizontal Floating-Gate," *IEEE Electron Device Letters*, vol. 43, no. 3, pp. 442-445, Mar. 2022.

10. *Dongseok Kwon, *Gyuweon Jung, Wonjun Shin, **Yujeong Jeong**, Seongbin Hong, Seongbin Oh, Jaehyeon Kim, Jong-Ho Bae, Byung-Gook Park, and Jong-Ho Lee, "Efficient Fusion of Spiking Neural Networks and FET-type Gas Sensors for a Fast and Reliable Artificial Olfactory System," *Sensors and Actuators B: Chemical*, vol. 345, p. 130419, Oct. 2021.

11. Wonjun Shin, Daehee Kwon, Minjeong Ryu, Joowon Kwon, Seongbin Hong, **Yujeong Jeong**, Gyuweon Jung, Jinwoo Park, Donghee Kim, and Jong-Ho Lee, "Effects of IGZO Film Thickness on H_2S Gas Sensing

Performance: Response, Excessive Recovery, Low-frequency Noise, and Signal-to-Noise Ratio," *Sensors and Actuators B: Chemical*, vol. 344, p. 130148, Oct. 2021.

12. **Yujeong Jeong**, Seongbin Hong, Gyuweon Jung, Wonjun Shin, Jinwoo Park, Donghee Kim, Yong Seok Choi, Jong-Ho Bae, Byung Hee Hong, and Jong-Ho Lee, "Highly Stable Si MOSFET-type Humidity Sensor with Ink-Jet Printed Graphene Quantum Dots Sensing Layer," *Sensors and Actuators B: Chemical*, vol. 343, p. 130134, Sep. 2021.

13. *Dongseok Kwon, *Gyuweon Jung, Wonjun Shin, **Yujeong Jeong**, Seongbin Hong, Seongbin Oh, Jong-Ho Bae, Byung-Gook Park, and Jong-Ho Lee, "Low-power and Reliable Gas Sensing System Based on Recurrent Neural Networks," *Sensors and Actuators B: Chemical*, vol. 340, p. 129258, Aug. 2021.

14. Huaping Wang, Jianmin Ma, Jun Zhang, Yuezhan Feng, Mani Teja Vijjapu, Saravanan Yuvaraja, Sandeep G Surya, Khaled N Salama, Chengjun Dong, Yude Wang, Qin Kuang, Zamaswazi P Tshabalala, David E Motaung, Xianghong Liu, Junliang Yang, Haitao Fu, Xiaohong Yang, Xizhong An, Shiqiang Zhou, Baoye Zi, Qingju Liu, Mario Urso, Bo Zhang, AA Akande, Arun K Prasad, Chu Manh Hung, Nguyen Van Duy, Nguyen Duc Hoa, Kaidi Wu, Chao Zhang, Rahul Kumar, Mahesh Kumar, Youngjun Kim, Jin Wu, Zixuan Wu, Xing Yang, SA Vanalakar, Jingting Luo, Hao Kan, Min Li, Ho Won Jang, Marcelo Ornaghi Orlandi, Ali Mirzaei, Hyoun Woo Kim, Sang Sub Kim, ASM Iftekhar Uddin, Jing Wang, Yi Xia, Chatchawal Wongchoosuk, Anindya Nag, Subhas Mukhopadhyay, Nupur Saxena, Pragati Kumar, Jing-Shan Do, Jong-Ho Lee, Seongbin Hong, **Yujeong Jeong**, Gyuweon Jung, Wonjun Shin, Jinwoo Park, Mara Bruzzi, Chen Zhu, Rex E Gerald, and Jie Huang, "Gas Sensing Materials Roadmap," *Journal of Physics: Condensed Matter*, vol. 33, no. 30, p. 303001, Jul. 2021.

15. Gyuweon Jung, Seongbin Hong, **Yujeong Jeong**, Wonjun Shin, Jinwoo

Park, Donghee Kim, Jong-Ho Bae, Byung-Gook Park, and Jong-Ho Lee, "Response Comparison of Resistor-and Si FET-Type Gas Sensors on the Same Substrate," *IEEE Transactions on Electron Devices*, vol. 68, no. 7, pp.3552-3557, Jul. 2021.

16. Wonjun Shin, Seongbin Hong, **Yujeong Jeong**, Gyuweon Jung, Jinwoo Park, Donghee Kim, Byung-Gook Park, and Jong-Ho Lee, "Optimization of Post-Deposition Annealing Temperature for Improved Signal-to-Noise Ratio in In_2O_3 Gas Sensor," *Semiconductor Science and Technology*, vol. 36, no. 7, p. 075007, Jul. 2021.
17. *Gyuweon Jung, *Wonjun Shin, Seongbin Hong, **Yujeong Jeong**, Jinwoo Park, Donghee Kim, Jong-Ho Bae, Byung-Gook Park, and Jong-Ho Lee, "Comparison of the Characteristics of Semiconductor Gas Sensors with Different Transducers Fabricated on the Same Substrate," *Sensors and Actuators B: Chemical*, vol. 335, p. 129661, May 2021.
18. Gyuweon Jung, Yoonki Hong, Seongbin Hong, Dongkyu Jang, **Yujeong Jeong**, Wonjun Shin, Jinwoo Park, Donghee Kim, Chan Bae Jeong, Dong Uk Kim, Ki Soo Chang, and Jong-Ho Lee, "A Low-power Embedded Poly-Si Micro-heater for Gas Sensor Platform Based on a FET Transducer and Its Application for NO_2 Sensing, *Sensors and Actuators B: Chemical*, vol. 334, p. 129642, May 2021.
19. Wonjun Shin, Seongbin Hong, **Yujeong Jeong**, Gyuweon Jung, Jinwoo Park, Donghee Kim, Chayoung Lee, Byung-Gook Park, and Jong-Ho Lee, "Effect of Charge Storage Engineering on the NO_2 Gas Sensing Properties of a WO_3 FET-type Gas Sensor with a Horizontal Floating-Gate," *Nanoscale*, vol. 13, no. 19, pp. 9009-9017, May 2021.
20. *Seongbin Hong, *Meile Wu, *Yoonki Hong, **Yujeong Jeong**, Gyuweon Jung, Wonjun Shin, Jinwoo Park, Donghee Kim, Dongkyu Jang, and Jong-Ho Lee, "FET-type Gas Sensors: A Review," *Sensors and Actuators B: Chemical*, vol. 330, p. 129240, Mar. 2021.

21. Wonjun Shin, Seongbin Hong, Gyuweon Jung, **Yujeong Jeong**, Jinwoo Park, Donghee Kim, Dongkyu Jang, Byung-Gook Park, and Jong-Ho Lee, "Improved Signal-to-Noise-Ratio of FET-type Gas Sensors using Body Bias Control and Embedded Micro-heater," *Sensors and Actuators B: Chemical*, vol. 329, p. 129166, Feb. 2021.

22. *Wonjun Shin, *Gyuweon Jung, Seongbin Hong, **Yujeong Jeong**, Jinwoo Park, Donghee Kim, Dongkyu Jang, Dongseok Kwon, Jong-Ho Bae, Byung-Gook Park, and Jong-Ho Lee, "Proposition of Deposition and Bias Conditions for Optimal Signal-to-Noise-Ratio in Resistor- and FET-type Gas Sensors," *Nanoscale*, vol. 12, no. 38, Oct. 2020.

23. *Wonjun Shin, *Gyuweon Jung, Seongbin Hong, **Yujeong Jeong**, Jinwoo Park, Dongkyu Jang, Byung-Gook Park, and Jong-Ho Lee, "Low Frequency Noise Characteristics of Resistor- and Si MOSFET-type Gas Sensors Fabricated on the Same Si Wafer with In_2O_3 Sensing Layer," *Sensors and Actuators B: Chemical*, vol. 318, p. 128087, Sep. 2020.

24. Dongkyu Jang, Gyuweon Jung, **Yujeong Jeong**, Seongbin Hong, and Jong-Ho Lee, "Barometric Pressure Sensor with Air Pocket Integrated with MOSFETs on the Same Substrate," *Journal of Semiconductor Technology and Science*, vol. 20, no. 3, pp. 305-310, Jun. 2020.

25. Gyuweon Jung, **Yujeong Jeong**, Yoonki Hong, Meile Wu, Seongbin Hong, Wonjun Shin, Jinwoo Park, Dongkyu Jang, and Jong-Ho Lee, "SO_2 Gas Sensing Characteristics of FET- and Resistor-type Gas Sensors Having WO_3 as Sensing Material," *Solid-State Electronics*, vol. 165, p. 107747, Mar. 2020.

26. **Yujeong Jeong**, Seongbin Hong, Gyuweon Jung, Dongkyu Jang, Wonjun Shin, Jinwoo Park, Seung-Ik Han, Hyungtak Seo, and Jong-Ho Lee, "NO_2 Sensing Characteristics of Si MOSFET Gas Sensor Based on Thickness of WO_3 Sensing Layer," *Journal of Sensor Science and Technology*, vol. 29,

no. 1, pp. 14-18, Jan. 2020.

27. Yoonki Hong, Meile Wu, Jong-Ho Bae, Seongbin Hong, **Yujeong Jeong**, Dongkyu Jang, Jun Shik Kim, Cheol Seong Hwang, Byung-Gook Park, and Jong-Ho Lee, “A New Sensing Mechanism of Si FET-based Gas Sensor using Pre-bias,” *Sensors and Actuators B: Chemical*, vol. 302, p. 127147, Jan. 2020.

28. Seongbin Hong, Yoonki Hong, **Yujeong Jeong**, Gyuweon Jung, Wonjun Shin, Jinwoo Park, Jung-Kyu Lee, Dongkyu Jang, Jong-Ho Bae, and Jong-Ho Lee, “Improved CO Gas Detection of Si MOSFET Gas Sensor with Catalytic Pt Decoration and Pre-bias Effect,” *Sensors and Actuators B: Chemical*, vol. 300, p. 127040, Dec. 2019.

29. Seongbin Hong, Jongmin Shin, Yoonki Hong, Meile Wu, **Yujeong Jeong**, Dongkyu Jang, Gyuweon Jung, Jong-Ho Bae, and Jong-Ho Lee, “Humidity-sensitive Field Effect Transistor with In_2O_3 Nanoparticles as a Sensing Layer,” *Journal of Nanoscience and Nanotechnology*, vol. 19, no. 10, pp. 6656-6662, Oct. 2019.

30. **Yujeong Jeong**, Jongmin Shin, Yoonki Hong, Meile Wu, Seongbin Hong, Ki Chang Kwon, Seokhoon Choi, Taehyung Lee, Ho Won Jang, and Jong-Ho Lee, “Gas Sensing Characteristics of the FET-type Gas Sensor Having Inkjet-printed WS_2 Sensing Layer,” *Solid-State Electronics*, vol. 153, pp. 27-32, Mar. 2019.

31. Seongbin Hong, Jongmin Shin, Yoonki Hong, Meile Wu, Dongkyu Jang, **Yujeong Jeong**, Gyuweon Jung, Jong-Ho Bae, Ho Won Jang, and Jong-Ho Lee, “Observation of Physisorption in a High-performance FET-type Oxygen Gas Sensor Operating at Room Temperature,” *Nanoscale*, vol. 10, no. 37, Oct. 2018.

Conferences

1. Gyuweon Jung, Jaehyeon Kim, Wonjun Shin, Seongbin Hong, **Yujeong Jeong**, Chayoung Lee, Woo Young Choi, and Jong-Ho Lee, "Innovative Gas Sensing Method Using Transient Behavior of FET-type Sensors with Gate Pulse Input," *2022 IEEE International Electron Devices Meeting (IEDM)*, Dec. 2022.
2. **Yujeong Jeong**, Seongbin Hong, Gyuweon Jung, Wonjun Shin, Woo Young Choi, and Jong-Ho Lee, "H_2S Sensing Characteristics of the Amplifier Circuit Consisting of *p*FET-type and Resistor-type Gas Sensors," *2022 International Conference on Solid State Devices and Materials (SSDM)*, Sep 2022.
3. Gyuweon Jung, Wonjun Shin, Hunhee Shin, Seongbin Hong, **Yujeong Jeong**, Kangwook Choi, Jinwoo Park, Donghee Kim, Chayong Lee, Jaehyeon Kim, Woo Young Choi, and Jong-Ho Lee, "Comparison of the H_2S gas response characteristics of semiconductor gas sensors (HFGFET-, TFT-, and resistor-type) fabricated on the same wafer," *2022 International Conference on Solid State Devices and Materials (SSDM)*, Sep 2022.
4. Kangwook Choi, Gyuweon Jung, Seongbin Hong, **Yujeong Jeong**, Wonjun Shin, Jinwoo Park, Chayong Lee, Donghee Kim, and Jong-Ho Lee, "Response Analysis of Resistor-Type Gas Sensor with Bias Voltage Condition," *2022 International Symposium on Olfaction and Electronic Nose (ISOEN)*, May 2022.
5. Gyuweon Jung, Jaehyeon Kim, Wonjun Shin, Seongbin Hong, **Yujeong Jeong**, Jinwoo Park, Donghee Kim, Kangwook Choi, and Jong-Ho Lee, "Optimal Bias Conditions for FET-Type Gas Sensors to Minimize Current Fluctuations," *2022 International Symposium on Olfaction and Electronic Nose (ISOEN)*, May 2022.
6. Wonjun Shin, Seongbin Hong, **Yujeong Jeong**, Gyuweon Jung, Byung-

Gook Park, and Jong-Ho Lee, "Highly Improved NO_2 Gas Sensing Performances Using Charge Storage Engineering in FET-type Gas Sensor with Embedded Micro-heater," *2022 Spring Conference of the Korean Sensors Society*, Apr. 2022.

7. **Yujeong Jeong**, Seongbin Hong, Gyuweon Jung, Wonjun Shin, Byung-Gook Park, and Jong-Ho Lee, "Comparison of the H_2S Sensing Characteristics of the Amplifier Circuits Consisting of the FET-type Gas Sensors with Different Load," *2022 Spring Conference of the Korean Sensors Society*, Apr. 2022.
8. Seongbin Hong, **Yujeong Jeong**, Gyuweon Jung, Wonjun Shin, Jinwoo Park, Donghee Kim, Chayoung Lee, Kangwook Choi, Jun Shik Kim, Cheol Seong Hwang, and Jong-Ho Lee, "Capacitor-Based Gas Sensor with a ZnO Sensing Layer," *The 29th Korean Conference on Semiconductors (KCS)*, Jan. 2022.
9. Jinwoo Park, Seongbin Hong, **Yujeong Jeong**, Gyuweon Jung, Wonjun Shin, Donghee Kim, Chayoung Lee, and Jong-Ho Lee, "Effects of Annealing Temperature on Stability of FET-type Gas Sensor," *The 29th Korean Conference on Semiconductors (KCS)*, Jan. 2022.
10. Kangwook Choi, Gyuweon Jung, Seongbin Hong, **Yujeong Jeong**, Wonjun Shin, Jinwoo Park, Donghee Kim, Jong-Ho Bae, Byung-Gook Park, and Jong-Ho Lee, "Response Analysis of Resistor-type Gas Sensor with Read Bias Condition," *The 29th Korean Conference on Semiconductors (KCS)*, Jan. 2022.
11. Seongbin Hong, **Yujeong Jeong**, Gyuweon Jung, Wonjun Shin, Jinwoo Park, Donghee Kim, Chayoung Lee, Kangwook Choi, and Jong-Ho Lee, "Long-term Degradation Characteristics of Gas Response depending on Deposition Atmosphere of Sensing Layer in FET-type Gas Sensors," *2021 Fall Conference of the Korean Sensors Society*, Oct. 2021.
12. **Yujeong Jeong**, Seongbin Hong, Gyuweon Jung, Wonjun Shin, Chayoung

Lee, Jinwoo Park, Donghee Kim, Kangwook Choi, and Jong-Ho Lee, "NO_2 Sensing Characteristics of the Amplifier Circuit Consisting of the FET-type Gas Sensors with FET Load," *2021 Fall Conference of the Korean Sensors Society*, Oct. 2021.

13. Seongbin Hong, **Yujeong Jeong**, Gyuweon Jung, Wonjun Shin, Jinwoo Park, Donghee Kim, Chayoung Lee, and Jong-Ho Lee, "Gas Sensing Performance of a Gated Lateral pnp-Bipolar Junction Transistor Gas Sensor Having a Horizontal Floating-Gate Structure," *2021 International Conference on Solid State Devices and Materials (SSDM)*, Sep. 2021.
14. **Yujeong Jeong**, Wonjun Shin, Seongbin Hong, Gyuweon Jung, Chayoung Lee, Jinwoo Park, Donghee Kim, and Jong-Ho Lee, "Amplifier Circuit Consisting of the FET-type Gas Sensors with Tunable FET Load," *2021 International Conference on Solid State Devices and Materials (SSDM)*, Sep. 2021.
15. Wonjun Shin, Byeongchan Choi, Junmo Lee, Seongbin Hong, **Yujeong Jeong**, Gyuweon Jung, Jinwoo Park, Donghee Kim, Chayoung Lee, and Jong-Ho Lee, "Sub-ppm Detection of NO_2 Gas using IGZO TFT-type Gas Sensor with Optimal Signal-to-Noise Ratio," *2021 International Conference on Solid State Devices and Materials (SSDM)*, Sep. 2021.
16. Wonjun Shin, Byeongchan Choi, Junmo Lee, Seongbin Hong, **Yujeong Jeong**, Gyuweon Jung, Jinwoo Park, Donghee Kim, Chayoung Lee, and Jong-Ho Lee, "Effects of Oxygen Flow Rate on the NO_2 Gas Sensing and Low-frequency Noise Characteristics in IGZO Gas Sensors," *The 19th International Nanotech Symposium & Exhibition*, Jul. 2021.
17. Donghee Kim, Jiseong Im, Seongbin Hong, **Yujeong Jeong**, Gyuweon Jung, Wonjun Shin, Jinwoo Park, and Jong-Ho Lee, "A Spiking Neural Network for Time-Efficient Gas Concentration Level Estimation in Resistor-Type Gas Sensors," *2021 Summer Annual Conference of IEIE*, Jun. 2021.

18. Seongbin Hong, **Yujeong Jeong**, Gyuweon Jung, Wonjun Shin, Jinwoo Park, Donghee Kim, and Jong-Ho Lee, "Macroscopic Analysis and Design of Si HFGFET Gas Sensor for Sensitive Gas Detection," *The 28th Korean Conference on Semiconductors (KCS)*, Jan. 2021.

19. Wonjun Shin, Joowon Kwon, Daehee Kwon, Minjeong Ryu, Seongbin Hong, **Yujeong Jeong**, Gyuweon Jung, Jinwoo Park, Donghee Kim, and Jong-Ho Lee, "Effect of Post-Deposition Annealing Atmosphere on NO_2 Gas Sensing and Low-frequency Noise in IGZO Thin-film Chemiresistor Gas Sensor," *The 28th Korean Conference on Semiconductors (KCS)*, Jan. 2021.

20. **Yujeong Jeong**, Seongbin Hong, Gyuweon Jung, Wonjun Shin, Jinwoo Park, Donghee Kim, and Jong-Ho Lee, "Effects of Oxygen Gas Flow on the Response of FET-type Gas Sensor with Sputtered WO_3 Sensing Layer," *The 28th Korean Conference on Semiconductors (KCS)*, Jan. 2021.

21. Gyuweon Jung, Seongbin Hong, **Yujeong Jeong**, Wonjun Shin, Jinwoo Park, Donghee Kim, Jong-Ho Bae, Byung-Gook Park, and Jong-Ho Lee, "H_2S Gas Sensing Characteristics of Si FET-type Gas Sensor with Localized Micro-heater," *The 28th Korean Conference on Semiconductors (KCS)*, Jan. 2021.

22. Jinwoo Park, Seongbin Hong, **Yujeong Jeong**, Gyuweon Jung, Wonjun Shin, Donghee Kim, and Jong-Ho Lee, "H_2S Gas Sensing Properties in Polysilicon Control-Gate FET Gas Sensor," *The 28th Korean Conference on Semiconductors (KCS)*, Jan. 2021.

23. Donghee Kim, Wonjun Shin, Seongbin Hong, **Yujeong Jeong**, Gyuweon Jung, Jinwoo Park, and Jong-Ho Lee, "Effect of Sensing Layer Length on H_2S Gas Sensing and Low-frequency Noise in Resistor-type Gas Sensor," *The 28th Korean Conference on Semiconductors (KCS)*, Jan. 2021.

24. Wonjun Shin, Seongbin Hong, **Yujeong Jeong**, Gyuweon Jung, Jinwoo Park, Dongseok Kwon, Dongkyu Jang, Donghee Kim, Byung-Gook Park,

and Jong-Ho Lee, “Efficient Improvement of Sensing Performance Using Charge Storage Engineering in Low Noise FET-type Gas Sensors,” *2020 IEEE International Electron Devices Meeting (IEDM)*, Dec. 2020.

25. **Yujeong Jeong**, Wonjun Shin, Seongbin Hong, Gyuweon Jung, Jinwoo Park, Dongkyu Jang, Donghee Kim, Dongseok Kwon, Byung-Gook Park, and Jong-Ho Lee, “Highly Sensitive Amplifier Circuit Consisting of Complementary pFET-type and Resistor-type Gas Sensors,” *2020 IEEE International Electron Devices Meeting (IEDM)*, Dec. 2020.
26. Wonjun Shin, Seongbin Hong, **Yujeong Jeong**, Gyuweon Jung, Jinwoo Park, Donghee Kim, Byung-Gook Park, and Jong-Ho Lee, “Effect of Post-Deposition Annealing Temperature on H_2S Sensing and Low-Frequency Noise Characteristics of In_2O_3 Gas Sensor,” *2020 International Conference on Solid State Devices and Materials (SSDM)*, Sep. 2020.
27. Donghee Kim, Wonjun Shin, Seongbin Hong, **Yujeong Jeong**, Gyuweon Jung, Jinwoo Park, Dongkyu Jang, Byung-Gook Park, and Jong-Ho Lee, “Effect of Bias Condition on the Gas Response in Resistor- and FET-type Gas Sensors,” *2020 Summer Annual Conference of IEIE*, Aug. 2020.
28. Jinwoo Park, Gyuweon Jung, Seongbin Hong, **Yujeong Jeong**, Wonjun Shin, Donghee Kim, Byung-Gook Park, and Jong–Ho Lee, “NO_2 Gas Sensing Properties in FET-type Gas Sensor having Horizontal Floating-Gate,” *2020 Summer Annual Conference of IEIE*, Aug. 2020.
29. Seongbin Hong, **Yujeong Jeong**, Gyuweon Jung, Wonjun Shin, Jinwoo Park, Jung-Kyu Lee, Dongkyu Jang, and Jong-Ho Lee, “Highly Sensitive and Selective Gas Sensing Performance in MOSFET-Based Gas Sensor Using Facile Metal Nanoparticle Agglomeration Process,” *The 27th Korean Conference on Semiconductors (KCS)*, Feb. 2020.
30. Jinwoo Park, Seongbin Hong, **Yujeong Jeong**, Gyuweon Jung, Wonjun Shin, Dongkyu Jang, and Jong-Ho Lee, “Effects of Body Bias and Operation Region on Gas Response in FET-type Gas Sensor having

Horizontal Floating-Gate," *The 27th Korean Conference on Semiconductors (KCS)*, Feb. 2020.

31. Wonjun Shin, Gyuweon Jung, Seongbin Hong, **Yujeong Jeong**, Jinwoo Park, Dongkyu Jang, and Jong-Ho Lee, "Effect of Resistor-type Gas Sensor Scaling on Sensing and Low frequency Noise Characteristics," *The 27th Korean Conference on Semiconductors (KCS)*, Feb. 2020.

32. **Yujeong Jeong**, Seongbin Hong, Gyuweon Jung, Dongkyu Jang, Wonjun Shin, Jinwoo Park, Seung-Ik Han, Hyungtak Seo, and Jong-Ho Lee, "Sensing Characteristics of the MOSFET-type Gas Sensor with Sputtered WO_3 Sensing Layer," *The 27th Korean Conference on Semiconductors (KCS)*, Feb. 2020.

33. Dongkyu Jang, Gyuweon Jung, **Yujeong Jeong**, Yoonki Hong, Seongbin Hong, Wonjun Shin, Ki Soo Chang, Chan Bae Jeong, Byung-Gook Park, and Jong-Ho Lee, "Efficient Integration of Si FET-type Gas Sensors and Barometric Pressure Sensors on the Same Substrate," *2019 IEEE International Electron Devices Meeting (IEDM)*, Dec. 2019.

34. Gyuweon Jung, Yoonki Hong, Seongbin Hong, **Yujeong Jeong**, Wonjun Shin, Jinwoo Park, Jung-Kyu Lee, Dongkyu Jang, and Jong-Ho Lee, "Detection of Low Concentration NO_2 Gas Using Si FET-Type Gas Sensor with Localized Micro-Heater for Low Power Consumption," *2019 IEEE Sensors*, Oct. 2019.

35. Dongkyu Jang, Yoonki Hong, Seongbin Hong, **Yujeong Jeong**, Gyuweon Jung, and Jong-Ho Lee, "Barometric Pressure Sensor with Air Pockets Fabricated by CMOS Process Technology," *2019 International Conference on Solid State Devices and Materials (SSDM)*, Sep. 2019.

36. Seongbin Hong, **Yujeong Jeong**, Yoonki Hong, Gyuweon Jung, Wonjun Shin, Jinwoo Park, and Jong-Ho Lee, "A Comparative Study on Gas Sensing Characteristics in Si MOSFET Gas Sensor Platform based on Integrated Sensing Mechanisms," *2019 Fall Conference of the Korean*

Sensors Society, Aug. 2019.

37. Gyuweon Jung, Yoonki Hong, Seongbin Hong, **Yujeong Jeong**, Wonjun Shin, Jinwoo Park, Jungkyu Lee, Dongkyu Jang, and Jong-Ho Lee, "Gas Sensing Characteristics of the Horizontal Floating-Gate FET-type Gas Sensor Deposited with In_2O_3 Film," *2019 Fall Conference of the Korean Sensors Society*, Aug. 2019.

38. Jong-Ho Lee, Seongbin Hong, Yoonki Hong, **Yujeong Jeong**, Gyuweon Jung, Wonjun Shin, Jinwoo Park, Dongkyu Jang, and Jung-Kyu Lee, "Sensing Mechanisms and Micro-Heater in Gas Sensors," *2019 IEEE International Conference on Circuits, Systems and Devices (ICCSD)*, Aug. 2019.

39. Jinwoo Park, **Yujeong Jeong**, Yoonki Hong, Seongbin Hong, Gyuweon Jung, Wonjun Shin, Jung-kyu Lee, Byung-Gook Park, and Jong–Ho Lee, "Effect of Body Bias on Gas Response in FET-type Gas Sensor having Horizontal Floating-Gate," *2019 Summer Annual Conference of IEIE*, Jun. 2019.

40. Wonjun Shin, Gyuweon Jung, **Yujeong Jeong**, Seongbin Hong, Jinwoo Park, Yoonki Hong, Byung-Gook Park, and Jong-Ho Lee, "The Effects of Operating Temperature on Field Effect Transistor Gas Sensor with In_2O_3 Sensing Layer," *2019 Summer Annual Conference of IEIE*, Jun. 2019.

41. Gyuweon Jung, Hyeongsu Kim, **Yujeong Jeong**, Yoonki Hong, Meile Wu, Seongbin Hong, Dongkyu Jang, Wonjun Shin, and Jong-Ho Lee, "Accurate Identification of Gas Type and Concentration using DNN Reflecting the Sensing Properties of MOSFET-type Gas Sensor," *2019 International Symposium on Olfaction and Electronic Nose (ISOEN)*, May 2019.

42. Jong-Ho Lee, **Yujeong Jeong**, Yoonki Hong, Meile Wu, Seongbin Hong, Gyuweon Jung, and Wonjun Shin, "High Performance Gas Sensor Platform Based on Integrated Sensing Mechanisms," *2019 International Conference on Semiconductor Technology for Ultra Large Scale Integrated Circuits and*

Thin Film Transistors (ULSIC vs. TFT 7), May 2019.

43. Yoonki Hong, Seongbin Hong, Dongkyu Jang, **Yujeong Jeong**, Meile Wu, Gyuweon Jung, Jun Shik Kim, Ki Soo Chang, Chan Bae Jeong, Cheol Seong Hwang, Byung-Gook Park, and Jong-Ho Lee, “A Si FET-type Gas Sensor with Pulse-driven Localized Micro-heater for Low Power Consumption,” *2019 Spring Conference of the Korean Sensors Society*, Mar. 2019.

44. **Yujeong Jeong**, Yoonki Hong, Seongbin Hong, Gyuweon Jung, Wonjun Shin, Jinwoo Park, Yong-Sahm Choe, Deok Hwan Yun, and Jong-Ho Lee, “NO_2 Sensing Characteristics of SnO_2 Gas Sensor depending on Operating Temperature,” *2019 Spring Conference of the Korean Sensors Society*, Mar. 2019.

45. Jinwoo Park, Seongbin Hong, Yoonki Hong, Meile Wu, **Yujeong Jeong**, Gyuweon Jung, Wonjun Shin, Dongkyu Jang, and Jong-Ho Lee, “Optimization of Measurement Condition for Improved Gas Sensing Characteristics in FET-Type Gas Sensor,” *2019 Spring Conference of the Korean Sensors Society*, Mar. 2019.

46. Seongbin Hong, Yoonki Hong, Meile Wu, **Yujeong Jeong**, Gyuweon Jung, Dongkyu Jang, Wonjun Shin, and Jong-Ho Lee, “Gas Sensing Characteristics of MOSFET Gas Sensor with Pillar-Shaped Horizontal Floating-Gate,” *The 26th Korean Conference on Semiconductors (KCS)*, Feb. 2019.

47. Gyuweon Jung, **Yujeong Jeong**, Yoonki Hong, Meile Wu, Seongbin Hong, Wonjun Shin, Dongkyu Jang, and Jong-Ho Lee, “The SO_2 Gas Sensing characteristics of WO_3 Deposited MOSFET Gas Sensor,” *The 26th Korean Conference on Semiconductors (KCS)*, Feb. 2019.

48. Yoonki Hong, **Yujeong Jeong**, Meile Wu, Seongbin Hong, Gyuweon Jung, Dongkyu Jang, and Jong-Ho Lee, “Sensing Characteristics of Si FET-type Humidity Sensor Having a WO_3 Sensing Layer by Using Pulse Scheme,”

2019 International Conference on Electronics, Information, and Communication (ICEIC), Jan. 2019.

49. Yoonki Hong, Seongbin Hong, Dongkyu Jang, **Yujeong Jeong**, Meile Wu, Gyuweon Jung, Jong-Ho Bae, Jun Shik Kim, Ki Soo Chang, Chan Bae Jeong, Cheol Seong Hwang, Byung-Gook Park, and Jong-Ho Lee, "A Si FET-type Gas Sensor with Pulse-driven Localized Micro-heater for Low Power Consumption," *2018 IEEE International Electron Devices Meeting (IEDM)*, Dec. 2018.
50. Seongbin Hong, Yoonki Hong, Meile Wu, **Yujeong Jeong**, Gyuweon Jung, Dongkyu Jang, Wonjun Shin, and Jong-Ho Lee, "Optimization of Horizontal Floating-Gate for Improved Gas Sensing Characteristics in FET-Type Gas Sensor," *2018 Annual Conference of the Korean Sensors Society*, Nov. 2018.
51. **Yujeong Jeong**, Yoonki Hong, Meile Wu, Seongbin Hong, Dongkyu Jang, Gyuweon Jung, and Jong-Ho Lee, "NO_2 Sensing Characteristics of Si FET-type Gas Sensor Having a WO_3 Sensing Layer," *2018 Annual Conference of the Korean Sensors Society*, Nov. 2018.
52. Seongbin Hong, Jongmin Shin, Yoonki Hong, Meile Wu, **Yujeong Jeong**, Jong-Ho Bae, and Jong-Ho Lee, "A Novel FET-type Hydrogen Gas Sensor with Pd-decorated Single-Walled Carbon Nanotubes by Electroplating Method," *The 17th International Meeting on Chemical Sensors (IMCS)*, Jul. 2018.
53. **Yujeong Jeong**, Jongmin Shin, Yoonki Hong, Meile Wu, Seongbin Hong, Dongkyu Jang, Ki Chang Kwon, Seokhoon Choi, Ho Won Jang, and Jong-Ho Lee, "Suppression of Drift in FET-type Gas Sensor Having WS_2 Nanoparticles Using Pulse Measurement," *The 17th International Meeting on Chemical Sensors (IMCS)*, Jul. 2018.
54. Seongbin Hong, Jongmin Shin, Yoonki Hong, Meile Wu, Dongkyu Jang, **Yujeong Jeong** and Jong-Ho Lee, "Humidity-sensitive Field Effect

Transistor with In_2O_3 Nanoparticles as a sensing layer," *The 25th Korean Conference on Semiconductors (KCS)*, Feb. 2018.

55. **Yujeong Jeong**, Jongmin Shin, Yoonki hong, Meile Wu, Seongbin Hong, and Jong-Ho Lee, "Gas Sensing Characteristics of the FET-type Gas Sensor Having Inkjet-printed WS_2 Sensing Layer," *The 25th Korean Conference on Semiconductors (KCS)*, Feb. 2018.

56. Seongbin Hong, Jongmin Shin, Yoonki Hong, Meile Wu, Dongkyu Jang, **Yujeong Jeong**, Hyuck-In Kwon, and Jong-Ho Lee, "Si FET-type Gas Sensor with a Horizontal Floating Gate Structure for Detecting Carbon Monoxide," *2017 Annual Conference of the Korean Sensors Society*, Nov. 2017.

57. Meile Wu, Jongmin Shin, Yoonki Hong, Dongkyu Jang, Seongbin Hong, **Yujeong Jeong**, and Jong-Ho Lee, "An FET-type Sensor with Pt Doped In_2O_3 Nanoparticles for Room Temperature Hydrogen Sensing," *2017 Annual Conference of the Korean Sensors Society*, Nov. 2017.

58. **Yujeong Jeong**, Jongmin Shin, Yoonki Hong, Meile Wu, Seongbin Hong, and Jong-Ho Lee, "Common Source Amplifier Circuit Integrated with the Gas Sensor," *2017 Annual Conference of the Korean Sensors Society*, Nov. 2017.